Electronic structure and bonding in thermoelectric skutterudites

Øystein Prytz

Thesis submitted in partial fulfillment
of the requirements for the degree of
Philosophiae Doctor

Department of Physics
University of Oslo

June 2007

Series of dissertations submitted to the
Faculty of Mathematics and Natural Sciences, University of Oslo.
No. 640

ISSN 1501-7710

Cover: Inger Sandved Anfinsen.
Printed in Norway: AiT e-dit AS, Oslo, 2007.

Produced in co-operation with Unipub AS.
The thesis is produced by Unipub AS merely in connection with the
thesis defence. Kindly direct all inquiries regarding the thesis to the copyright
holder or the unit which grants the doctorate.

Unipub AS is owned by
The University Foundation for Student Life (SiO)

Ich und Mich sind immer zu eifrig im Gespräche: wie wäre es auszuhalten, wenn es nicht einen Freund gäbe?
- Friedrich Nietzsche, Also sprach Zarathustra.

Summary

The present work is a study of the electronic structure and bonding of the class of materials often called skutterudites. These materials have received much attention during the past decade, largely because their thermoelectric properties are rather easily modified and improved. Most investigations have been into synthesizing materials and measuring their thermoelectric properties. There have also been several theoretical studies of their electronic structure. However, there have been fewer experimental studies of the bonding of these materials. In this thesis, electron energy-loss spectroscopy and x-ray photoelectron and Auger spectroscopy have been used together with density functional calculations to study the electronic structure of skutterudites. This combination of experimental and theoretical methods may be mutually beneficial, and the aim of this thesis is to bridge the gap between theoretical considerations and experimental investigations of the bonding.

Acknowledgments

There is a saying due to John Donne, 'No man is an island', but as this is a rather trite thing to say when acknowledging help and support received, I'll refrain from using it. It is nonetheless true. This thesis would never have come about without the constant interaction I have had with a lot of wonderful people. First and foremost my supervisors, Johan Taftø, Helmer Fjellvåg, and Terje Finstad, deserve thanks for their scientific input and support. I would in particular like to thank Johan for excellent supervision and enthusiasm for my project, not to mention the endless and fun discussions about everything between heaven and earth.

There are several other people with whom I have collaborated closely, their input and suggestions have been invaluable. Ole Martin Løvvik and Krister Mangersnes have contributed greatly to the scientific output with DFT calculations and discussion. Spyros Diplas has been central to the XPS work, but his enthusiasm alone is worthy of mention! Ole Bjørn Karlsen has been indispensable for the synthesis work, and Sissel Jørgensen deserves great thanks for help around the lab. Furthermore Channing Ahn and Brent Fultz of Caltech have contributed with a lot of interesting discussions and input to much of the EELS work. Thank you all!

The people who have contributed scientifically to this thesis are important, but just as important are all the people who have not! I am of course talking about friends and family. First I would like to thank my mother and father. I don't know how they did it, but they managed to stir my interest for science and technology at quite an early age, encouraging me to stick with it throughout all my 21 years of education. Furthermore I would like to thank Olav for friendly heckling, Klaus and Ingvild for endless (no really, endless!) discussions of research and education policy, Annett, Tor Helge, and Kanutte for being good friends, and Mariam, Håkon, and Tone for many wonderful dinners and a very welcome diversion from a social life otherwise dominated by physicists. Finally I would like to give a big hug and thanks to Martin and Daniel for being my very best friends over many, many years.

Øystein Prytz
June 2007

Preface

Work on this thesis started in the autumn of 2003, and has been funded by the University of Oslo through the FUNMAT@UiO programme. The major part of the research was carried out at the Department of Physics, under the supervision of professors Johan Taftø, Helmer Fjellvåg, and Terje Finstad. The main focus of the work has been on studies of the electronic structure of skutterudites using electron energy-loss spectroscopy, density functional theory, and x-ray photoelectron and Auger spectroscopy.

During the spring of 2006, I spent three months at the California Institute of Technology performing EELS experiments under the guidance of Channing C. Ahn and Brent Fultz. The work done during my stay there is presented in Paper III of this thesis. A further month was spent at Brookhaven National Labs doing energy filtered electron diffraction experiments in collaboration with Yimei Zhu and Lijun Wu; this is still work in progress and is not presented here.

In addition to the work done in direct relation to my Ph.D. project, I have participated in several other projects that have resulted in publications that are not part of this thesis. These are listed below.

- Ø. Prytz and J. Taftø. Accurate determination of domain boundary orientation in $LaNbO_4$. *Acta Materialia* **53**, 297 (2005).
- U. Olsbye, A. Virnovskaia , Ø. Prytz *et al.* Mechanistic Insight in the Ethane Dehydrogenation reaction over Cr/Al_2O_3 catalysts. *Catalysis Letters* **103**, 143 (2005).
- A. Virnovskaia, S. Jørgensen, J. Hafizovic, Ø. Prytz *et al.* In situ XPS investigation of Pt(Sn)/ Mg(Al)O catalysts during ethane dehydrogenation experiments. *Surface Science* **601**, 30 (2007).
- K. Mangersnes, O. M. Løvvik, and Ø. Prytz. Optimization of P-based skutterudites for thermoelectricity from first principles calculations. Submitted to *Physical Review B* (2007).
- Ø. Prytz, R. Sæterli, and J. Taftø. Comparison of the electronic structure of a thermoelectric skutterudite before and after adding rattlers: an electron energy loss study. Submitted to *Micron* (2007).

Table of Contents

List of Figures

Chapter 1

Introduction

The choice of thermoelectric materials as the topic of this Ph.D. study is largely motivated by the challenges related to energy and environment. The past decade has seen increasing concern about the world energy supply. Today, the world energy consumption is more than twenty times higher than in 1900. This increase has mainly occurred in the industrialized part of the world, and is seen as a necessity for a modern lifestyle. As the 3rd World economies grow and their standards of living increase, their energy use will nearly double by 2030 [1]. Indeed, the total world consumption is expected to increase by almost 60% from 2004 to 2030, and most of this increase will take place outside the OECD [1].

The burning of fossil fuels has for most of the 20th century accounted for a majority of the energy supply, contributing more than 80% of the consumption in 2004 [1]. This is the cause of major environmental concern as evidence suggests that emission of large amounts of CO_2 is causing heating of the atmosphere, in addition to the environmental damage caused by NO_x and SO_x released in the burning of fossil fuels.

In light of the expected increase in energy consumption and growing environmental concerns, there is increased interest for alternative sources of energy and the technology for their use. Most industrialized countries have large programmes focused on developing and implementing new, environmentally friendly and renewable sources of energy. Although a handful of technologies, such as photovoltaics and biofuels, have received the most public attention, one can expect that a plethora of technologies will need to be implemented in all sectors of the economy.

However, the criteria for successful implementation of new energy technologies are not easily met. To be deemed both politically and economically acceptable, the new technologies must be capable of supporting dramatic increases of living standards in the less developed world, moderate increases in living standards in the western world, and both of these with less damage to the environment and at lower costs than today's petroleum based technology.

Dresselhaus and Thomas have reviewed some possible alternative sources for energy [2], and recently the United Nations Energy Programme reported that investments in sustainable energy jumped by 40% from 2005 to 2006 [3]. The total world investments now exceed $70 billion, and the growth is expected to continue into 2007. Although this is encouraging, one should not be too optimistic about large scale exploitation of alternative sources of energy in the short term. The technology and economy of many of these sources are still far from adequate, and fossil fuels are expected to play a major role in supplying the world with the energy needed for decades to come. It is therefore important to consider if already extant energy resources can be exploited more efficiently, and with less harm to the environment.

In the past decade, there has been a resurgence in interest in thermoelectric materials and devices [4]. In applications of thermoelectricity, the coupling between electric currents and heat flow are exploited. This allows a thermoelectric device to function either as a heat pump to transport heat when an electric current is applied, or as a generator when the device is placed in a temperature gradient. Use of thermoelectric devices may therefore facilitate a more efficient use of energy, or at least the option of recuperating some of the energy lost to waste heat in e.g. industrial processes.

Extensive research efforts have gone into investigating these possibilities, and developing new materials for such applications [4, 5]. Although the prospects of using thermoelectric devices as a part of new and more efficient energy production and use are promising, there have so far been few applications in this regard. The main bottleneck is the efficiency of the existing materials, and this is the focus of intense research in the fields of physics, chemistry, and materials science.

In the present work, the electronic structure and bonding of the so-called skutterudite materials have been studied. These materials have received much attention during the past decade, largely because their thermoelectric properties are rather easily modified and improved [6]. Most investigations have been into synthesizing materials and measuring their thermoelectric properties. There have also been several theoretical studies of their electronic structure. However, there have

been fewer experimental studies of the bonding of these materials. In this thesis, electron energy-loss spectroscopy and x-ray photoelectron and Auger spectroscopy have been used together with density functional calculations to study the electronic structure. This combination of experimental and theoretical methods may be mutually beneficial, and the aim of this thesis is to bridge the gap between theoretical considerations and experimental investigations of the bonding.

References

[1] International energy outlook 2007. Tech. Rep. DOE/EIA-0484(2007), Energy Information Administration/US Department of Energy, Washington DC (2007).

[2] Dresselhaus, M. S. & Thomas, I. L. Alternative energy technologies. *Nature* **414**, 332 (2001).

[3] Global trends in sustainable energy investment 2007. Tech. Rep. ISBN: 978-92-807-2859-0, DTI/0985/PA, United Nations Environment Programme (2007).

[4] Chen, G., Dresselhaus, M. S., Dresselhaus, G., Fleurial, J. P. & Caillat, T. Recent developments in thermoelectric materials. *International Materials Review* **48**, 45 (2003).

[5] Riffat, S. & Ma, X. Thermoelectrics: a review of present and potential applications. *Applied Thermal Engineering* **23**, 913 (2003).

[6] Uher, C. Skutterudites: Prospective novel thermoelectrics. *Semiconductors and semimetals* **69**, 139 (2001).

Chapter 2

Thermoelectricity and its applications

In this chapter, a background on the thermoelectric effect and a simple model for the thermopower α of a material are presented. The figure of merit is introduced, and furthermore a brief review of the current status of thermoelectric materials is given. Finally, possible applications of thermoelectric materials as heat pumps and generators of electrical power are discussed.

2.1 The thermoelectric effect

The discovery of the thermoelectric effect is often attributed to Thomas Johann Seebeck who in 1821 observed that an electric current flows through a circuit made of two different materials, if the two junctions are kept at different temperatures. Another aspect of the same physical phenomenon was observed somewhat later (1834) by Jean-Charles-Athanase Peltier. Working with similar circuits as Seebeck, he discovered that passing a current through the two materials caused heat to be absorbed at one junction and expelled at the other.

2.1.1 Simple classical model

These effects, today known as the Seebeck and Peltier effects, are both caused by a coupling of the currents of heat and electrical charge. If one realizes that e.g. electrons are carriers of

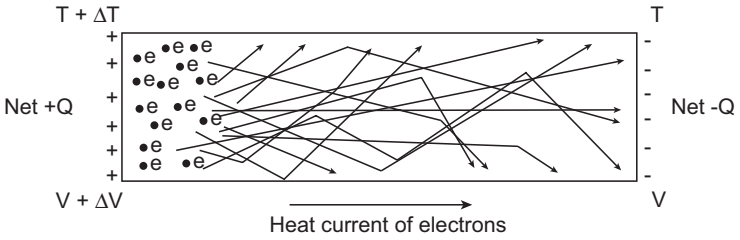

Figure 2.1: *An intuitive model of the diffusion of electrons caused by a temperature gradient. An electrically isolated slab of material is heated on the left ($\Delta T > 0$) causing a net flux of electrons towards the right. Adapted from Lovell [1].*

both heat and charge, the existence of such effects may not be too surprising. Indeed, a simple classical picture of an electrically isolated slab of material, such as that shown in figure 2.1, may suffice as a first intuitive explanation of the phenomenon.

At finite temperatures, we can consider the electrons as particles which are continually in motion in random directions. If the two ends of the material are in thermal equilibrium ($\Delta T = 0$), the probability of an electron making its way from one end to the other is the same as for an electron traveling the opposite direction. Thus, there will be no net flux of electrons.

However, if one end is at a higher temperature than the other, the thermally induced motion of the electrons there will be more vigorous than on the cold side. If this is the case, there will be a net flux of charge from the hot to the cold side.

This process will continue until the induced electric potential between the two ends is large enough to halt the net flow of electrons, and a stationary state is achieved. The Seebeck coefficient (or thermopower) of the material is then phenomenologically defined as the ratio of the potential difference to the temperature difference:

$$\alpha = \frac{\Delta V}{\Delta T} \tag{2.1}$$

For a material where electrons are the dominant charge carrier, as in figure 2.1, if $\Delta T > 0$ then ΔV is a negative number and the Seebeck coefficient is also negative. Conversely, in this simple classical model the thermopower is positive if positively charged holes are the dominant carrier.

Although this model may be sufficient to gain a first intuitive understanding of the phenomenon, the transport properties of materials can not be fully understood classically. In the next section, a simple non-classical model for the thermopower of a material is presented.

2.1.2 Evaluation of the Seebeck coefficient

This derivation roughly follows that of Dugdale [2]. The perhaps easiest way to evaluate the Seebeck coefficient is though the related Peltier coefficient. In doing this, an electric field E_x is applied in the x-direction of a material which is held at a constant temperature. The Peltier coefficient π is given as the ratio between the heat current density relative to the electrical current density, and is related to the Seebeck coefficient α through the Kelvin relation [3]:

$$\pi = \frac{\text{heat current}}{\text{electrical current}} = \frac{j_x^Q}{j_x^e} = T\alpha \tag{2.2}$$

Under the assumption that all transport of heat and charge is in the x-direction and is solely determined by the flow of electrons—that is no heat or charge transport by holes, and no heat is carried by phonons—the current densities of heat and electrical charge are given by:

$$j_x^Q = \frac{1}{V}\sum_i h_i v_i(x) \tag{2.3}$$

$$j_x^e = \frac{1}{V}\sum_i e v_i(x) \tag{2.4}$$

Here e is the electron charge and $v_i(x)$ is the electron velocity in the x-direction, while the sum is over all electrons i and V the volume of the system. In order for a transport of heat to occur, an electron must be thermally excited at one end of the material, only to lose this energy in a de-excitation process after being moved some distance by the applied electrical field. The heat transported into a unit volume is given by the thermodynamic identity: $\mathrm{d}Q = T\mathrm{d}S = \mathrm{d}U - \mu\mathrm{d}N$ where $\mathrm{d}U$ is the change in internal energy, $\mathrm{d}S$ is the change in entropy, μ the chemical potential, and $\mathrm{d}N$ is the change in number of particles in the volume. The heat introduced by one electron

is then $h_i = \varepsilon_i - \mu$, where ε_i is the energy of the thermally excited electron.

Combining equations (2.2) and (2.3) with this definition of the carried heat, an expression for the Seebeck coefficient can be found:

$$\alpha = \frac{\pi}{T} = \frac{1}{Te}\frac{\sum_i h_i v_i(x)}{\sum_i v_i(x)} = \frac{1}{Te}\frac{\sum_i (\varepsilon_i - \mu) v_i(x)}{\sum_i v_i(x)} \tag{2.5}$$

Furthermore, the current density contributed by the i'th electron in the x-direction is defined as $j_i^e(x) = e v_i(x)$, giving:

$$\alpha = \frac{1}{Te}\frac{\sum_i (\varepsilon_i - \mu) j_i^e(x)}{\sum_i j_i^e(x)} \tag{2.6}$$

It is often more convenient to deal with an integration over all energies instead of a sum over many electrons. If the contribution to the electric current by electrons with energy between ε and $\varepsilon + \mathrm{d}\varepsilon$ is described as $j_x^e(\varepsilon)\mathrm{d}\varepsilon$, equation (2.6) can be written [2]:

$$\alpha = \frac{1}{Te}\frac{\int (\varepsilon - \mu) j_x^e(\varepsilon)\mathrm{d}\varepsilon}{\int j_x^e(\varepsilon)\mathrm{d}\varepsilon} \tag{2.7}$$

The Seebeck coefficient can be further evaluated by examining $j_x(\varepsilon)$, which is the contribution to the current density of electrons with with energy ε. The total current density is then the integral of this partial density over all energies. It can be shown [2] that this is given by:

$$j_x = \int j_x(\varepsilon)\mathrm{d}\varepsilon = \int -E_x \sigma_x(\varepsilon)\frac{\mathrm{d}f_0(\varepsilon)}{\mathrm{d}\varepsilon}\mathrm{d}\varepsilon \tag{2.8}$$

where E_x is the applied electric field, and $\sigma_x(\varepsilon)$ is the conductivity of electrons with energy ε. Also, the equilibrium Fermi–Dirac distribution function $f_0(\varepsilon)$ has been introduced. The electric conductivity is to a large part determined by the number of available electrons for conduction and the scattering of electrons in the material. Both of these are dependent on energy, and it is therefore reasonable that the conductivity is a function of energy. Inserting this into equation (2.7) one arrives at:

$$\alpha = \frac{1}{Te}\frac{\int \frac{\mathrm{d}f_0(\varepsilon)}{\mathrm{d}\varepsilon}(\varepsilon-\mu)\sigma_x(\varepsilon)\mathrm{d}\varepsilon}{\int \frac{\mathrm{d}f_0(\varepsilon)}{\mathrm{d}\varepsilon}\sigma_x(\varepsilon)\mathrm{d}\varepsilon} \tag{2.9}$$

which is a well known expression for the Seebeck coefficient [4, 2, 5].

It is important to remember that this model is limited: it assumes that there is no contribution from holes to the electrical current and transport of heat, and also that the there are no phonons that carry heat. These are factors that can be incorporated into the model, but would complicate the derived expression quite a bit. Furthermore, it is important to be aware that all factors appearing in equation (2.9) are temperature dependent, and the expression is therefore only valid for situations where the heat transfer does not cause any changes in temperature.

Nevertheless, equation (2.9) gives a lot of important information on the thermopower. First, at energies far from the Fermi–level, f_0 is a constant (either 1 or 0). Thus, the appearance of derivative of the Fermi–Dirac function, $\frac{\mathrm{d}f_0(\varepsilon)}{\mathrm{d}\varepsilon}$, shows that only electrons close to the Fermi-level contribute. Furthermore, the function $\frac{\mathrm{d}f_0(\varepsilon)}{\mathrm{d}\varepsilon}(\varepsilon-\mu)$ is anti-symmetric about the Fermi–level and integrates to zero. Therefore, if non-zero values of α are to be obtained, the conductivity, $\sigma(\varepsilon)$ must be a non-symmetric function of energy. That is, the conductivity must vary for electrons of different energy. Indeed, it can be shown [2, 6] that the thermopower can be evaluated as

$$\alpha = \frac{\pi^2}{3}\frac{(k_B T)^2}{eT}\frac{1}{\sigma(\varepsilon)}\frac{\partial\sigma(\varepsilon)}{\partial\varepsilon}\Big|_{\varepsilon=\varepsilon_F} \tag{2.10}$$

where the appearance of the term $\frac{\partial\sigma(\varepsilon)}{\partial\varepsilon}$ emphasizes this point. Such a variation of the electric conductivity can be achieved for example if the the scattering processes and the density of states close to the Fermi–level (available electrons) varies strongly as a function of energy.

2.1.3 The figure of merit

The macroscopic equations of charge and heat transfer are now examined [4]. Consider a sample where the two ends are held at constant, but different, temperatures, giving a temperature gradient ∇T. This difference in temperature will cause a thermoelectric current $J_e^{\nabla T} = -\sigma\alpha\nabla T$ to flow

in the material. If an electric field E is applied, the total current density becomes:

$$J_e = J_e^E + J_e^{\nabla T} = \sigma E - \sigma\alpha\nabla T \tag{2.11}$$

with one contribution ($J_e^{\nabla T}$)arising from the temperature difference and, one from the electric field (J_e^E).

The thermal current density J_Q can be analyzed in a similar manner. At zero electric field, but in a temperature gradient, the thermal current density will be given by $J_Q^{\nabla T} = -\lambda_0\nabla T$, where λ_0 is the thermal conductivity at zero electric field. If an electric field is applied, the induced current of electrons will contribute to the thermal current through the term $J_Q^E = J_e^E\pi = J_e^E\alpha T$, and the total heat current will be given by:

$$J_Q = J_Q^E + J_Q^{\nabla T} = J_e^E\alpha T - \lambda_0\nabla T \tag{2.12}$$

There are two effects that have been ignored in these expressions. First, the internal resistance of the material will cause a heating effect I^2R, which can be disregarded for small currents. Secondly, the Thomson–effect is neglected, an approximation which is valid for small temperature differences or if the Seebeck coefficient is independent of temperature [4, 3].

From equation (2.11) an expression for the electric current caused in an external field is achieved:

$$J_e^E = J_e + \alpha\nabla T\sigma \tag{2.13}$$

which is insert into equation (2.12) to arrive at:

$$\begin{aligned} J_Q &= (J_e + \alpha\nabla T\sigma)\alpha T - \lambda_0\nabla T \\ &= \alpha J_e T + \alpha^2\sigma T\nabla T - \lambda_0\nabla T \\ &= \alpha T J_e + (\alpha^2\sigma T - \lambda_0)\nabla T \\ &= \alpha T J_e - \lambda_0(1 - \frac{\alpha^2\sigma}{\lambda_0}T)\nabla T \\ &= \pi J_e - \lambda\nabla T \end{aligned} \tag{2.14}$$

The final line of equation (2.14) shows that the total heat current is the sum of two contributions: one which depends on the Peltier coefficient and the electric current, and one which varies with the temperature gradient. In doing this, a new total thermal conductivity is defined that takes into account the retarding effect of the thermoelectrically induced electric field: $\lambda = \lambda_0(1 - \frac{\alpha^2\sigma}{\lambda_0}T) = \lambda_0 - \alpha^2\sigma T$. Rearranging this expression gives:

$$ZT = \frac{\alpha^2\sigma}{\lambda}T = \frac{\lambda_0}{\lambda} - 1 \tag{2.15}$$

where $Z = \frac{\alpha^2\sigma}{\lambda}$. This relationship is of particular importance when investigating the thermoelectric effect in materials. For example, if heat is to be transferred along the temperature gradient, it is obvious from equation (2.14) that the highest amount of heat transfer for a given electrical current is achieved for small values of λ. Equation (2.15) shows that this corresponds to large values of ZT.

Similarly, the maximum electric current for a given value of the temperature gradient can be investigated. Combining equations (2.14) and (2.12) gives:

$$\begin{aligned} J_Q = \pi J_e - \lambda\nabla T &= \sigma E\alpha T - \lambda_0\nabla T \\ \alpha T J_e &= \sigma E\alpha T - \lambda_0\nabla T + \lambda\nabla T \\ J_e &= \sigma E - \frac{(\lambda_0 - \lambda)}{\alpha T}\nabla T \end{aligned} \tag{2.16}$$

Thus, at $E = 0$, the maximum current $J_e^{max} = -\frac{\lambda_0}{\alpha T}\nabla T$ is achieved with small values [1] of λ, which corresponds to large values of ZT.

Because of its importance in determining how close the system is to an 'ideal' thermoelectric machine, ZT is often considered as the *figure of merit* for a thermoelectric material. Investigations into new thermoelectric materials often report this figure as their main result, and in section 2.2 a brief review of the state of current research into new materials is given. In general, commercially used materials today have a maximum figure of merit $ZT \approx 1$.

Through similar arguments as those leading to the relation between ZT and the thermal conductivities in equation (2.15), one can obtain [7] the expression $ZT = V_\alpha/V_\rho$ where V_α is the Seebeck voltage and V_ρ is the voltage drop due to the ohmic resistance of the material. Although this approach may allow a quick evaluation of a material in a single experiment, it is often preferable to separately measure the properties in equation (2.15), and thereby gain insight into their individual contributions to the figure of merit. This is particularly important when modifying materials in an attempt to improve their thermoelectric performance.

2.2 State of the art thermoelectric materials and the search for new compositions

Since thermoelectric phenomena were first observed, there has periodically been great interest in investigating the thermoelectric (TE) effect in various materials. As shown in the previous section, a 'good' TE material needs to have a high figure of merit, that is, a high value for the Seebeck coefficient, good electric conductivity, and low thermal conductivity. Some materials may possess one or more of these characteristics, however, further improvements in the figure of merit may be achieved through careful modifications of the material.

One obvious way of improving the figure of merit is if the Seebeck coefficient can be increased. From equation (2.9) we see that this can be achieved by ensuring a large gradient in the electric

[1] The function $|(\lambda_0 - \lambda)|$ has a maximum value of λ_0. This can be understood if one realizes that λ can not be larger than λ_0 (from equation (2.15)). Furthermore, λ can only take positive values, since a negative value of the thermal conductivity would allow a spontaneous transport of heat from the cold end of the material to the hot side. This is not possible, as it would cause a net reduction of the entropy of the system, thereby violating the Second Law of Thermodynamics.

conductivity, $\sigma(\varepsilon)$, close to the Fermi–level. Unfortunately, tuning the Seebeck coefficient in this manner will also affect the number of available conducting states, possibly giving a lower overall electric conductivity, which in turn is detrimental to the TE performance of the material. Conversely, modifying the electric conductivity $\sigma(\varepsilon)$ may have unwanted effects on the Seebeck coefficient.

The coupling between thermal and electric conductivities must also be considered. There are two contributions to the total thermal conductivity: the electron (λ_e) and lattice (λ_l) parts. Thus, the total thermal conductivity can then be written $\lambda = \lambda_e + \lambda_l$. The electron contribution is due to electrons carrying heat, and can be described by the Wiedemann–Franz law. This empirical law states that the electron contribution to the thermal conductivity can be described by the relation: $\lambda_e = L_0 \sigma T$, where L_0 is approximately a constant [8], and σ is the electric conductivity. The lattice contribution to the thermal conductivity is due to the heat carried by the lattice vibrations through quantized oscillations called phonons.

In materials with high electrical conductivity, λ_e dominates, and the thermal conductivity is often considered to be described solely by the Wiedemann–Franz law. For these materials, increasing the electric conductivity will cause a proportional increase in the thermal conductivity. Examining equation (2.15), one notes that this defeats the goal of increasing the figure of merit. Indeed, for a metal, where the Wiedemann–Franz law accurately describes the total thermal conductivity, the figure of merit becomes $ZT = \frac{\alpha^2}{L_0} T$ and depends only on the value of the Seebeck coefficient. Although there in principle is no upper bound for the value of ZT, for practical purposes the highest value will be achieved by striking a balance between several effects that may very well counteract each other.

Roughly, one can say that there have been three periods of research into TE materials. Early focus on the transport properties of metals revealed that while they have a high electric conductivity, their Seebeck coefficients are usually too small and their thermal conductivity too large for practical energy conversion or heat pump applications. After these initial investigations interest waned and there was little progress in developing new materials. It was only after the Second World War that the advent of modern semiconductors gave a renewed interest in thermoelectric phenomena in materials. These materials have a much larger Seebeck coefficient than metals, and, through doping, can achieve reasonable values of the electric conductivity. Furthermore, explorations of space created a demand for power sources which can operate unattended and without maintenance for long periods of time, without any significant deterioration in the

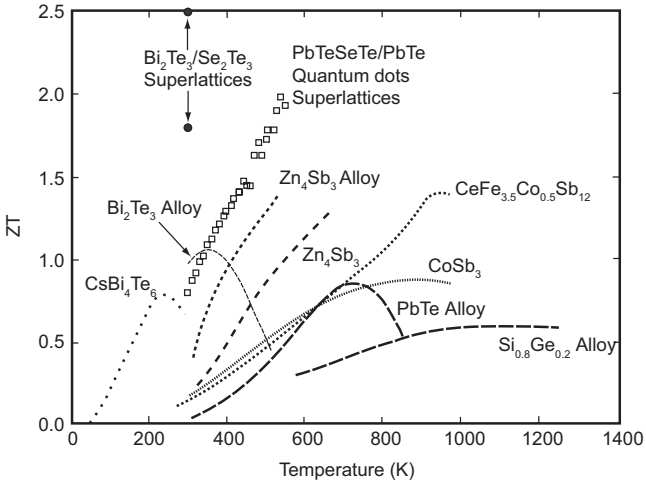

Figure 2.2: *The dimensionless figure of merit for several thermoelectric materials that have been investigated the last decade. Adapted from [9].*

amount of power supplied. As will be discussed in the next section, electric generators based on thermoelectric materials are prime candidates to fill such a niche. Up till the mid 1960's, a huge number of binary semiconductors were investigated, and this burst of research resulted in many of the thermoelectric materials that are used today. These include the Bi-Te alloys which have a $ZT \approx 1$ at room temperature, and the Si-Ge alloys which are suited to work at high temperatures.

The third bout of increased activity on thermoelectric materials started in the early 1990's. There are two main features of the recent activity that should be mentioned: first, the exact tuning of the electronic properties has been greatly aided through modern quantitative theory, such as calculations based on density functional theory (DFT). For example, through studies of the density of states and position of the Fermi–level it is possible to consider the above mentioned tradeoff between increasing the Seebeck coefficient and any concomitant reduction in electric conductivity.

Furthermore, researchers have endeavored to reduce the total thermal conductivity without at the same time causing a reduction in the electric conductivity. This can be achieved by modifications of the material that introduce defects or structural features that strongly scatter phonons, but have a smaller effect on the charge carriers. Thus, only the lattice part λ_l of the thermal conductivity

is affected, and changes in the electric conductivity are avoided. This can dramatically enhance the figure of merit for a material. For example, Bi_2Te_3/Sb_2Te_3 super-lattices have been reported to achieve a room temperature figure of merit up to 2.4, which is significantly higher than that of similar bulk materials [10].

Figure 2.2 shows the figure of merit ZT as a function of temperature for some of the most recently investigated materials, as well as the 'old' bulk semiconductors which are commercially available. It is important to note that any given material only achieves its maximum figure of merit for a certain temperature region. Outside this range, the figure of merit declines, or perhaps the material decomposes at higher temperatures. Thus, for any application, the material has to be selected based on the operating temperature of the device.

2.3 Applications

The coupling of electric and thermal currents in a material allows for several interesting applications. By applying a current, one can achieve a heat pump effect giving heating or cooling, while naturally occurring temperature gradients or waste heat can be used to generate electricity. Thermoelectric materials have seen some success in applications where special conditions dictate that conventional methods of heating/cooling or power generation cannot be utilized. In general, TE devices are of particular interest due to their compact and low weight nature. In addition, unlike most other technologies, TE devices have few or no moving parts, and the need for mechanical maintenance is therefore usually very low. However, there have so far been only limited commercial success in consumer goods and large scale applications. This may change with the increasing focus on environmentally friendly power use and generation, and as more efficient TE materials are being developed.

2.3.1 Heat pump effect: cooling and heating

First, the use of TE materials as heat pumps is investigated. For most applications, two different TE materials are combined in a TE device, or thermocouple. A sketch of such a device is shown in figure 2.3. The two materials used are e.g. semiconductors doped in such a way that one is an n-type conductor, while the other is p-type. The materials are connected electrically in series,

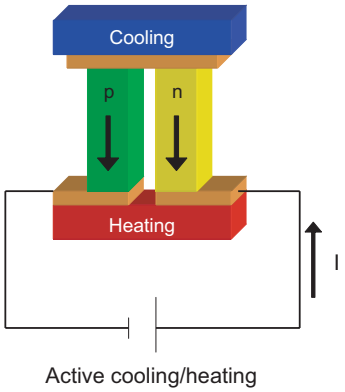

Figure 2.3: *Sketch of a thermoelectric device (thermocouple) operating as a heat pump. The two legs are made of different materials, one with n-type conductivity and one with p-type. The legs are connected electrically in series and thermally in parallel. An external power source sets up an electrical current though the device, thus causing a net flux of heat.*

but thermally in parallel. Applying a voltage will set up a current as shown in the figure, driving charge carriers from one end of the device to the other. As the charge carriers are also carriers of heat, this will cause a cooling of one end and heating of the other.

The rate of heat absorption at the cold end is given by

$$\dot{Q} = \alpha(T_m - \frac{\Delta T}{2})I - \frac{1}{2}I^2R - \lambda_0 \Delta T \tag{2.17}$$

where T_m is the average temperature in the device and ΔT is the temperature difference. This expression is analogous to equation (2.12), however, the Joule heating I^2R caused by the electric current and the internal ohmic resistance of the material is now also taken into account. It can be assumed that half of this heat ends up at the cold end, thereby reducing the rate of cooling. The Thomson effect is neglected as it is very small compared to the effects under consideration here. The cooling efficiency can be defined as the rate of heat transport for a given power input. The power input is given by $W = \alpha \Delta T I + I^2R$, where the first term is the power needed to overcome the Seebeck voltage arising from the temperature difference, while the second is the power loss due to ohmic resistance in the device.

The cooling efficiency ϕ then becomes

$$\phi_{cooling} = \frac{\dot{Q}}{W} = \frac{\alpha(T_m - \frac{\Delta T}{2})I - \frac{1}{2}I^2R - \lambda_0 \Delta T}{\alpha \Delta T I + I^2 R} \tag{2.18}$$

In order to achieve maximum efficiency, there are two factors that need to be considered. First, the geometry of the thermocouple must be optimized so as to minimize power loss due to Joule heating and losses from return heat conduction due to the temperature gradient. Second, there is an optimum current for which the heat transport is maximum with regard to the heating I^2R. For a thermocouple satisfying these conditions, it can be shown [3] that the cooling efficiency is given by

$$\phi_{cooling} = \frac{T_m(\sqrt{1 + ZT_m} - 1)}{\Delta T(\sqrt{1 + ZT_m} + 1)} - \frac{1}{2} \tag{2.19}$$

Here T_m is the mean temperature across the thermocouple, while Z is the figure of merit of the device defined in a similar manner as in equation (2.15).

The highest cooling efficiency is achieved when the temperature difference between the two sides is relatively small, however, the overall efficiency of a TE cooling device is usually far lower than for gas-compression based technology. For example, a typical household refrigerator operates in a 20° temperature difference between room temperature ($\approx$ 300 K) and somewhat above freezing. With values of $ZT \approx 1$, this will give an efficiency of approximately 1.4 for the TE device. In comparison, conventional compressor based refrigerators have an efficiency of 2–4 under similar operating conditions [9]. For a TE refrigerator to achieve this level of efficiency, thermoelectric materials with a value of ZT around 3–4 would be needed.

Despite this rather low efficiency, TE refrigeration has become rather commonplace in special applications where traditional cooling technologies are impractical. The perhaps most visible application to the general public is the use of portable TE picnic coolers intended for use in e.g. cars. Traditional cooling with compression/decompression of a cooling liquid is usually infeasible for such applications due to volume and weight restrictions. However, this is only one of many applications that take advantage of the light weight and compactness of TE cooling technology. Other advantages that often make TE cooling more attractive than the other alternatives

are localized and highly controllable cooling, noiseless operation, and very low maintenance needs.

In some cases, the reverse application of the heat-pump may be of more interest. Instead of using the TE device for cooling, one can consider the possibility of using the heat pump effect to achieve heating, for example to heat houses or offices by transporting heat from the outside to the inside. The physics of this process are very similar to that of the case for cooling, except that the Joule heat produced by the electric current is no longer a detrimental effect. Instead of reducing the efficiency, the I^2R heating now contributes to the desired result, meaning that the sign of the $\frac{1}{2}I^2R$ term in equation (2.17) should be changed. The heating efficiency now becomes [3] $\phi_{heating} = \phi_{cooling} + 1$ giving

$$\phi_{heating} = \frac{T_m(\sqrt{1+ZT_m}-1)}{\Delta T(\sqrt{1+ZT_m}+1)} + \frac{1}{2} \tag{2.20}$$

Assuming a 20° temperature difference, and a room temperature of 295 K, the heating efficiency is close to 3 for a TE device with $ZT_m \approx 1$. The efficiency is largest for small temperature differences, meaning that if the outside temperature drops too much, the benefit of such a heat pump compared to conventional heating is reduced.

2.3.2 Power generation

An alternative application of the thermoelectric phenomenon is to take advantage of the voltage caused by a temperature gradient. For example, thermoelectric devices are widely used as accurate temperature sensors. However, in the following, the focus is on use of thermoelectric materials for power genereneration.

For power generation, thermoelectric materials are combined in a device in a similar manner as for heating/cooling applications. The device is then placed in a temperature gradient which may originate from for example solar or geothermal sources, or from industrial waste heat. The difference in temperature causes an electric current to flow, thereby converting some of the thermal energy to electric energy, see figure 2.4.

The conversion efficiency is the fraction of heat input that is converted to electricity, and can be

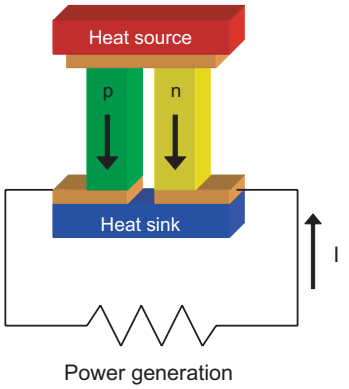

Figure 2.4: *Thermocouple in power generation mode*

shown [3] to depend on the temperature difference and the figure of merit of the device through the relation

$$\eta = \frac{T_1 - T_2}{T_1} \frac{\sqrt{1 + ZT_m} - 1}{\sqrt{1 + ZT_m} + T_2/T_1} \tag{2.21}$$

where T_1 and T_2 are the hot and cold side side temperatures respectively. In contrast to the situation where we wish to achieve heating or cooling, the maximum efficiency is now obtained for large temperature differences.

Thermoelectric generator based on this principle have been in use for several decades. The perhaps most well known applications are as power sources for space probes launched by the US and Soviet Union. This power source is particularly interesting for deep space probes that operate far from the Sun, and therefore cannot rely on photovoltaics for their power. Instead, heat is supplied by the decay of a radioactive isotope, and some of this heat is converted to electricity by the TE device. Several well known space missions, such as Voyager and Viking, have relied on this technology for their power. In all, more than 50 space probes have used TE generators as their main sources of power [11].

Terrestrial applications are not uncommon. In particular, thermoelectric generators are used for powering electric equipment located in remote areas that do not have access to the electrical grid,

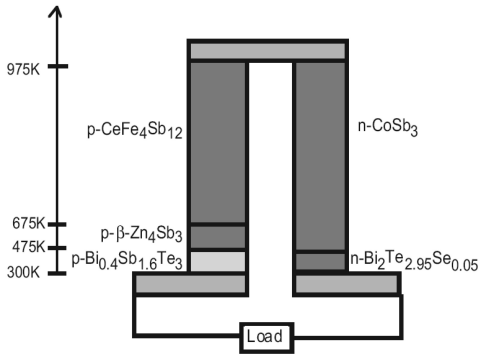

Figure 2.5: *Example of a proposed segmented thermocouple in which different materials are used depending on the temperature variation throughout the device [13]. The predicted conversion efficiency of this device is 15.5% with a hot side temperature of 975 K and cold side temperature of 300 K.*

or where frequent maintenance is impractical. These applications include powering meteorological equipment or other sensors, cathodic protection of pipelines, and telecommunication devices. The needed heat is usually supplied by burning of fossil fuels [12].

The conversion efficiency of these devices is usually in the range of 4–9% [12]. However, by increasing the temperature difference, it would be possible to achieve a higher conversion rate. For example, from equation (2.21) one finds that a hot side temperature of 900 K and cold side temperature of 300 K would give a conversion efficiency of approximately 15% if the figure of merit is $ZT_m \approx 1$.

However, it is not a trivial matter to obtain such conversion rates. As seen in the previous section, each thermoelectric material has a certain temperature range over which it has favourable properties. If a TE device is designed with materials suitable for the hot side temperature, these materials will most likely not be able to operate optimally at the cold end. In other words, ZT for any one material is far from optimal for the entire range of temperatures throughout the device. Thus, the efficiency cited above would probably not be possible with any single device/material.

Several possible solutions to this problem have been proposed. One possibility is to construct the TE device from several materials which are suited to different temperatures. Closest to the hot side, one would use materials suited for high temperatures, while closer to the cold side other

materials would be used. An example of such a device is sketched in figure 2.5. The predicted conversion efficiency of this device is 15.5% with a hot side temperature of 975 K and cold side temperature of 300 K [13, 14], thus rivaling the efficiency of commercial photovoltaic cells.

In conclusion, thermoelectric materials have great potential as electric generators or heat pumps, especially if their figure of merit ZT can be raised above that of the currently available commercial materials. This is a field of intense and growing research activity world wide, although great challenges remain.

References

[1] Lovell, M. C., Avery, A. J. & Vernon, M. W. *Physical Properties of Materials* (Van Nostrand Reinhold Company, New York, 1976).

[2] Dugdale, J. S. *The Electrical Properties of Metals and Alloys*. The Structure and Properties of Solids 5 (Edward Arnold, London, 1977).

[3] Goldsmid, H. J. *Applications of thermoelectricity* (Methuen & Co. Ltd., London, 1960).

[4] Mahan, G. D. Good Thermoelectrics. In Eherenreich, H. & Spaepen, F. (eds.) *Solid State Physics, vol. 51*, 82–152 (Academic Press, San Diego, 1998).

[5] Cutler, M. & Mott, N. F. Observation of Anderson Localization in an Electron Gas. *Physical Review* **181**, 1336 (1969).

[6] Ashcroft, N. W. & Mermin, N. D. *Solid State Physics* (Thomson Learning, Saunders College, Philadelphia, 1976).

[7] Harman, T. C. Special Techniques for Measurement of Thermoelectric Properties. *Journal of Applied Physics* **29**, 1373 (1958).

[8] Kittel, C. *Introduction to Solid State Physics* (John Wiley & Sons, Inc., 1996), 7th edn.

[9] Chen, G., Dresselhaus, M. S., Dresselhaus, G., Fleurial, J. P. & Caillat, T. Recent developments in thermoelectric materials. *International Materials Review* **48**, 45 (2003).

[10] Venkatasubramanian, R., Siivola, E., Colpitts, T. & O'Quinn, B. Thin-flm thermoelectric devices with high room-temperature fgures of merit. *Nature* **413**, 597–602 (2001).

[11] Bennett, G. L. Space applications. In Rowe, D. M. (ed.) *CRC Handbook of Thermoelectrics*, chap. 41, 515–537 (CRC Press, Boca Raton, 1995).

[12] McNaughton, A. G. Commercially available generators. In Rowe, D. M. (ed.) *CRC Handbook of Thermoelectrics*, chap. 36, 459–469 (CRC Press, Boca Raton, 1995).

[13] Caillat, T., Fleurial, J. P., Snyder, G. J. & Borshchevsky, A. Development of high efficiency segmented thermoelectric unicouples. In *Proceedings of the 20th International Conference on Thermoelectrics, Beijing*, 282. IEEE (IEEE catalog no. TH8589, 2001).

[14] Caillat, T. *et al.* A new high efficiency segmented thermoelectric unicouple. In *Proceedings of the 34th Intersociety Energy Conversion Engineering Conference*, 2567 (Vancouver, 1999).

Chapter 3

Skutterudites

In this chapter, materials with the skutterudite-like structure are presented. Their crystal structure, bonding and physical properties are discussed. Particular emphasis is put on modifications of the materials that lead to enhanced thermoelectric properties.

3.1 Crystal structure and bonding in binary skutterudites

The binary skutterudite compounds have the general chemical formula MX_3, where M typically is one of the column 9 transition metal (Co, Rh, or Ir), and X is one of the elements P, As, or Sb (often called pnicogen). The skutterudites belong to the cubic space group $Im\bar{3}$ (no. 204), and their unit cell may be considered to consist of eight smaller cubes with metals atoms on the corners. Six of these cubes are filled with mutually perpendicular (nearly square) rectangles made up of the X atoms, while two of the cubes are left empty, see figure 3.1(a). The pnicogens are located slightly off center in a tetrahedron of two pnicogen and two metal atoms (figure 3.1(b)), while the metal atoms are octahedrally coordinated by pnicogens (figure 3.1(c)). Thus, each pnicogen has two pnicogen and two metal nearest neighbours, while each metal has six pnicogen nearest neighbours.

Using Wyckoff notation, the metal atoms are placed on the 8c sites, the X atoms are on the 24g sites and the voids are the 2a sites. The structure is fully defined by the cell parameter a, and two

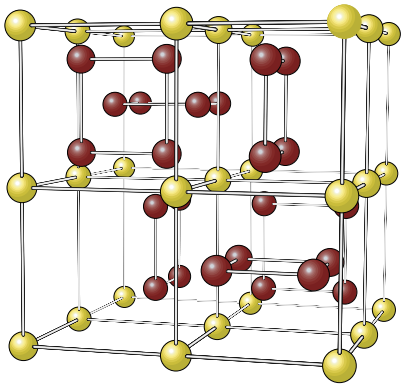

(a) The skutterudite unit cell with the rectangular pnicogen 'rings' emphasized.

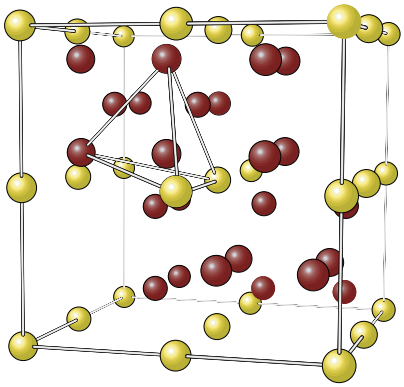

(b) The tetrahedral environment of the pnicogens. Each pnicogen has two pnicogen and two transition metal nearest neighbours.

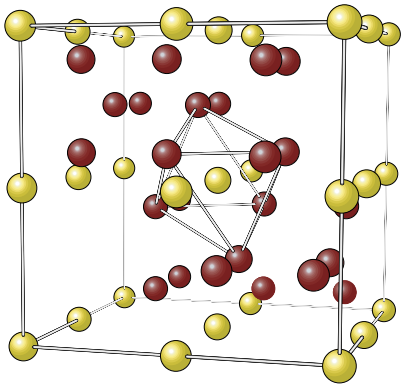

(c) The octahedral environment of the transition metal atoms.

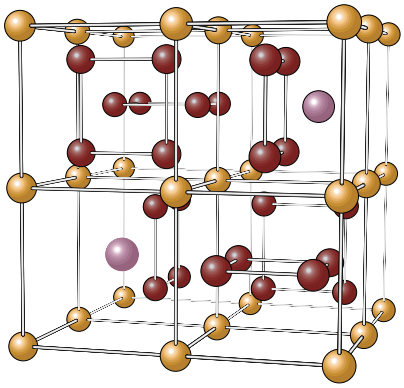

(d) The filled skutterudite structure. Here the transition metal has been fully substituted with a lower valent element (e.g. Fe) and a 'rattler' (in purple) introduced in the two large voids.

Figure 3.1: *The unit cell of the skutterudite structure with the origin translated [1/4 1/4 1/4], and the various structural features emphasized. The pnicogen atoms are shown in red, and the transition metals in yellow/gold.*

Table 3.1: *Structural parameters of some binary skutterudites.*

	a (Å)	y	z
CoP_3 ref. [1]	7.7112	0.34895	0.14513
$CoAs_3$ ref. [2]	8.195	0.3431	0.1503
$CoSb_3$ ref. [3]	9.0385	0.33537	0.15788
RhP_3 ref. [4]	7.9951	0.3547	0.1393
IrP_3 ref. [4]	8.0151	0.3540	0.1393

Table 3.2: *Comparison of the covalent radii of Co and P, As, and Sb [6] with the observed bond length in skutterudites [4].*

	Covalent radius r (pm)	$r_{Co} + r_X$		Observed Co-X bond length (pm)
Co	125			
P	110	235	CoP_3	222
As	121	246	$CoAs_3$	234
Sb	141	266	$CoSb_3$	252

positional parameters y and z for the pnicogens. Table 3.1 lists structural parameters for some binary skutterudites.

The bonding of skutterudites is often considered to be covalent in nature. First, the difference in electronegativity between the metal and pnicogen atoms is not large enough for the bonding to be considered ionic. As an example, the difference in electronegativity in an ionic compound such as CoO is approximately 1.5 (Pauling units), while for the most extreme case in skutterudite (CoP_3) the difference is only about 0.3 [5]. Thus, sharing of electrons in a covalent bond is expected in stead of transfer of charge between the elements. Furthermore, the observed M–X bond length is close to the sum of the elemental covalent radii. For example, the sum of covalent radii for Co and P is 235 pm, while the observed bond length in CoP_3 is slightly less at 222 pm, see table 3.2. This is comparable to the situation in e.g. GaAs. Thus covalent bonding is expected, although a slight ionic character is possible.

The valence electron configuration of the pnicogen atoms is of the type ns^2np^3, giving five available electrons for bonding. As shown in figure 3.1(b) each pnicogen has two pnicogen and two metal nearest neighbours. In a covalent model of bonding, two pnicogen valence electrons contribute to bonding with the nearest pnicogens, while the remaining three form bonds with the two metal atoms. From the perspective of the metal atom, the octahedral environment gives rise

to d^2sp^3 hybrid metal orbitals with octahedral symmetry. The metal atom donates three electrons towards these bonds, while the remaining nine are supplied by the pnicogens [4, 7].

Turning to the electronic structure calculated by density functional theory (DFT), the various skutterudite compounds show great similarities. As an example, the total density of states (DOS) and the symmetry projected local density of states for the three cobalt based skutterudites are shown in figure 3.2. The Co d states are split into states of t_{2g} and e_g symmetry due to the octahedral environment of the Co atoms, with the majority of the Co d states strongly peaked approximately 2-2.5 eV below the Fermi-level. The pnicogen p states are rather uniformly distributed above and below the Fermi-level, hybridizing with the Co d states and contributing heavily to the total DOS in the -7 to +5 eV region . The Co s and p states contribute only to a small degree to the total DOS, while the pnicogen s states dominate in the region 9-15 eV below the Fermi-level. In CoP_3, the Fermi-level is located at the very lower edge of the conduction band, while in $CoAs_3$ and $CoSb_3$ it is shifted slightly downwards towards the valence band, into a region where the density of states is very small. The presence of such a region with a low density of states is typical of the skutterudites [8, 9, 10], and is often referred to as a pseudo-gap. The calculated pseudo-gap is approximately 1 eV wide in CoP_3 and decreases in width in the skutterudites with the heavier pnicogens and larger unit cells.

Although the density of states is very low in this region, it is generally not found to be zero. This becomes seen most easily when the band structure is plotted. Figure 3.3 shows the band structure of CoP_3 near the Fermi-level, and it is evident that the pseudo-gap is crossed by a single band touching the conduction band near the Γ point just above the Fermi-level. Thus, theory predicts that CoP_3 is a metal. However, this contradicts experimental evidence indicating semiconducting behaviour of CoP_3 [12]. This may perhaps be explained by the tendency of DFT calculations to underestimate band gaps.

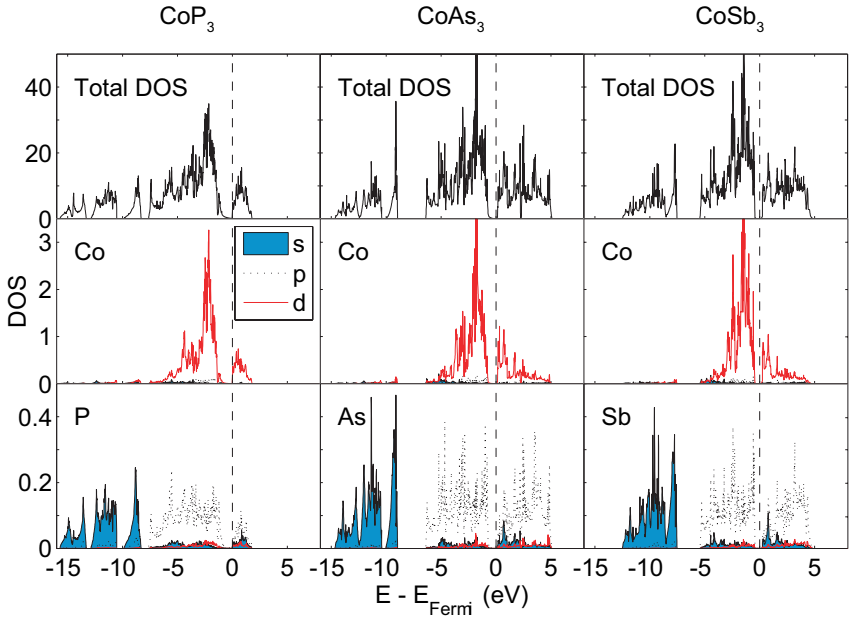

Figure 3.2: *The total and projected density of states for CoP_3, $CoAs_3$, and $CoSb_3$ [11].*

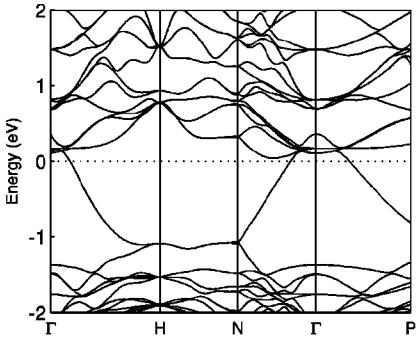

Figure 3.3: *CoP_3 band structure showing that a single band crosses the pseudo-gap close to the Γ point [13].*

3.2 Filled skutterudites and thermoelectric applications

Several binary skutterudite compounds have relatively high values of the Seebeck coefficient and the electrical conductivity. For example, values as high as 630 $\mu V/K$ have been reported for the Seebeck coefficient of $CoSb_3$ [14], which together with reasonable electric conductivity makes this compound interesting for thermoelectric applications. Unfortunately, the thermal conductivity of the skutterudites has been found to be too high, and only moderate values of the dimensionless figure of merit are usually achieved.

This changed, however, in 1994, when Slack and Tsoukala suggested that filling the the voids in the structure could reduce the thermal conductivity of the material through scattering of thermal phonons [15]. It has been known for decades that ternary skutterudites can be made [16], where additional atoms are placed in the large voids as in figure 3.1(d). In the case of a complete filling of the structure, the general formula is $R_yM_4X_{12}$ with $y = 1$. Here R is typically an electropositive rare earth metal.

Complete filling is, however, generally not achieved in compounds made with Co or another column 9 transition metals. Filling fractions for these materials are typically well below $y = 0.5$, with the case of Ba filled Cobalt–Antimony skutterudites with $y = 0.44$ considered an anomaly [14]. For example, the maximum filling fraction for $Ca_yCo_4Sb_{12}$ has been found to be $y = 0.2$ [17], and theoretical investigations suggest that the solubility of La, Y and Sc in CoP_3 is below $y = 0.06$ [13].

In order to achieve high levels of filling while maintaining structural stability, it is often necessary to perform a charge compensation, or doping, by substituting the transition metal with a lower valent element. The argument here is that the extra valence electrons brought into the system by the filling element are compensated for by reducing the number valence electrons contributed towards the metal–pnicogen bonding by the transition metal. Thus the octahedral metal–pnicogen complex becomes electron deficient relative to the situation in the binary skutterudite, and charge is transferred from the filling atom to compensate this deficiency. This allows large filling fractions, and even a complete filling of the structure [12, 16, 18].

Typical examples are the substitution of Co with Fe, which allows the complete filling of the voids. As an example, tetravalent Ce can participate in a $CeFe_4P_{12}$ skutterudite. Here each iron atom has one less valence electron than cobalt, and the Fe_4P_{12} complex can be considered

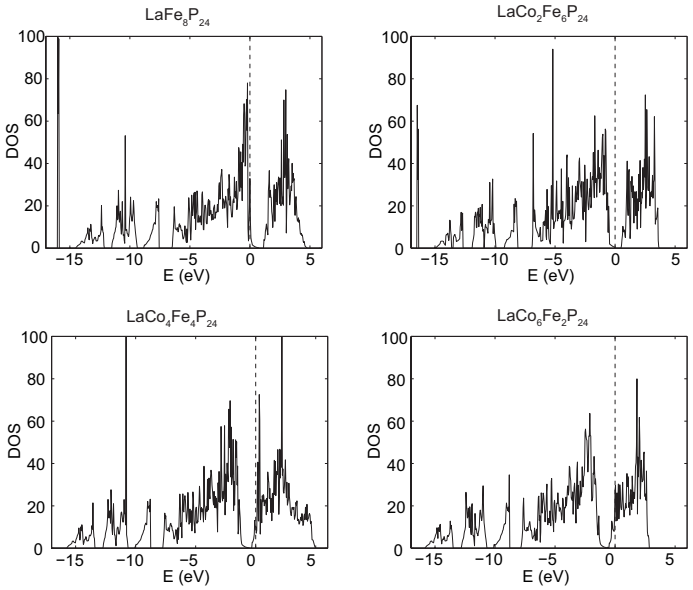

Figure 3.4: *The calculated DOS for various degrees of substitution in a fully La-filled phosphorus skutterudite [19]. Increasing the amount of Co in the structure relative to Fe causes the Fermi–level to move from the top of the valence band, across the pseudo-gap, and into the bottom of the conduction band.*

to lack four electron compared to an analogous Co_4P_{12} complex. However, this deficiency is exactly compensated for by the four valence electrons of Ce, and the chemical formula can be written $Ce^{4+}[Fe_4P_{12}]^{4-}$. Thus, whereas the metal–pnicogen bonding is usually considered to be covalent, cerium is assumed to be in a positively charged ionic state.

In addition to stabilizing the structure, substituting Fe for Co allows a tuning of the electronic structure and transport properties of the material. Figure 3.4 shows the calculated density of states for a series of filled P-based skutterudites [19]. Here the voids are completely filled with La, while the amount of substitution is varied. The general features of the DOS are very similar for the various compositions. However, for the completely substituted $La_2Fe_8P_{24}$ compound, the Fermi-level is located at the top of the valence band, while with lower degrees of substitution it moves across the pseudo-gap and into the conduction band. Thus, by varying the degree of substitution the electronic properties can to some extent be controlled. This is important since it allows for keeping the already beneficial electronic properties relatively unchanged while

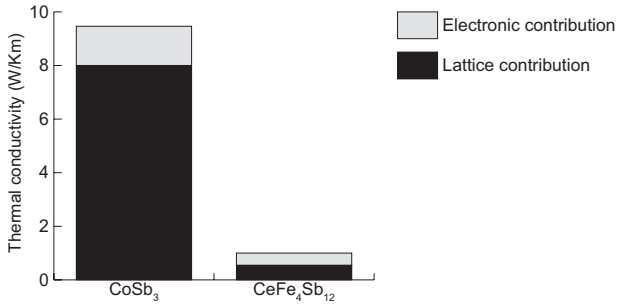

Figure 3.5: *The thermal conductivity of $CoSb_3$ and $CeFe_4Sb_{12}$ at 300 K. The lattice and electronic contributions have been estimated using the Wiedemann-Franz law and a Lorenz number $L_0 = 2.44 \cdot 10^{-8} \frac{W\Omega}{K^2}$. The data were adapted from refs. [22] and [24].*

modifying the structure.

The effect of this filling on the thermal conductivity has been thoroughly demonstrated with many different filling elements, typically the rare earth elements R=La, Ce, Nd, Sm, Eu, Th etc. Dramatic reductions in the thermal conductivity up to an order of magnitude have been observed [20, 21, 22, 18, 23]. For example, figure 3.5 shows the thermal conductivity of $CoSb_3$ compared to that of $CeFe_4Sb_{12}$. By using the Wiedemann–Franz law, the total thermal conductivity can be partitioned into a lattice and an electronic contribution. We see a dramatic reduction in the thermal conductivity of the filled and substituted compound compared to the unfilled one, with most of the reduction due to a reduction in the lattice contribution.

The rationale for this effect is that when the filler atoms are placed in the large voids in the structure, they are very loosely bound to their neighbours giving a very high thermal displacement parameter. That is, they "rattle" in an oversized box. Thus they serve as very efficient scatterers of thermal phonons, thereby lowering the thermal conductivity of the material. In addition, it is well documented that the maximum reduction in thermal conductivity is achieved for only a partial filling of the voids [22], indicating that scattering of phonons against randomly distributed point defects plays an important role. These point defects need not be the filling atoms, there have also been several studies, both experimental and theoretical, into the effect of various transition metal substitutions on the transport properties of the materials [25, 26, 27, 28]. Among other things, these studies indicate that point defect scattering of phonons against the substitution elements also play an important role in reducing the thermal conductivity of the crystal.

References

[1] Jeitschko, W. *et al.* Crystal structure and properties of some filled and unfilled skutterudites: $GdFe_4P_{12}$, $SmFe_4P_{12}$, $NdFe_4P_{12}$, $Eu_{0.54}Co_4Sb_{12}$, $Fe_{0.5}Ni_{0.5}P_3$, CoP_3 and NiP_3. *Zeitschrift für Anorganische und Allgemeine Chemie* **626**, 1112 (2000).

[2] Mandel, N. & Donohue, J. The refinement of the crystal structure of skutterudite, $CoAs_3$. *Acta Crystallographica B* **27**, 2288 (1971).

[3] Schmidt, T., Kliche, G. & Lutz, H. D. Structure Refinement of Skutterudite-Type Cobalt Triantimonide, $CoSb_3$. *Acta Crystallographica C* **43**, 1678 (1987).

[4] Uher, C. Skutterudites: Prospective novel thermoelectrics. *Semiconductors and semimetals* **69**, 139 (2001).

[5] Atkins, P. W. *Quanta – A Handbook of concepts* (Oxford University Press, Oxford, 1991), 2 edn.

[6] Shriver, D. F. & Atkins, P. W. *Inorganic Chemistry* (Oxford Univeristy Press, Oxford, 1999), 3 edn.

[7] Dudkin, L. D. The chemical bond in semiconducting cobalt triantimonide. *Soviet Physics - Technical Physics* **3**, 216 (1958).

[8] Llunell, M., Alemany, P., Alvarez, S., Zhukov, V. P. & Vernes, A. Electronic structure of skutterudite type phsophides. *Physical Review B* **53**, 10605 (1996).

[9] Fornari, M. & Singh, D. J. Electronic structure and thermoelectric properties of phosphide skutterudites. *Physical Review B* **59**, 9722 (1999).

[10] Koga, K., Akai, K., Oshiro, K. & Matsuura, M. Electronic structure and optical properties of binary skutterudite antimonides. *Physical Review B* **71**, 155119 (2005).

[11] Prytz, Ø., Løvvik, O. M. & Taftø, J. Comparison of theoretical and experimental dielectric functions: Electron energy-loss spectroscopy and density-functional calculations on skutterudites. *Physical Review B* **74**, 245109 (2006).

[12] Watcharapasorn, A. *et al.* Preparation and thermoelectric properties of some phosphide skutterudite compounds. *Journal of Applied Physics* **86**, 6213 (1999).

[13] Løvvik, O. M. & Prytz, Ø. Density-functional band-structure calculations for La-, Y-, and Sc-filled CoP_3 based skutterudite structures. *Physical Review B* **70**, 195119 (2004).

[14] Chen, L. D. *et al.* Anomalous barium filling fraction and n-type thermoelectric performance of $Ba_yCo_4Sb_{12}$. *Journal of Applied Physics* **90**, 1864 (2001).

[15] Slack, G. A. & Tsoukala, V. G. Some properties of semiconducting $IrSb_3$. *Journal of Applied Physics* **76**, 1665 (1994).

[16] Jeitschko, W. & Braun, D. $LaFe_4P_{12}$ with Filled $CoAs_3$-Type structure and Isotypic Lanthanoid-Transition Metal Polyphosphides. *Acta Crystallographica B* **33**, 3401 (1977).

[17] Puyet, M., Lenoir, B., Dauscher, A., Weisbecker, P. & Clarke, S. J. Synthesis and crystal structure of $Ca_xCo_4Sb_{12}$ skutterudites. *Journal of Solid State Chemistry* **177**, 2138 (2004).

[18] Sales, B. C., Mandrus, D., Chakoumakos, B. C., Keppens, V. & Thompson, J. R. Filled skutterudite antimonides: Electron crystals and phonom glasses. *Physical Review B* **56**, 56 (1997).

[19] Mangersnes, K. *Density functional calculations of skutterudites for thermoelectric applications*. Master's thesis, Department of Physics, University of Oslo, Oslo, Norway (2006).

[20] Sales, B. C., Mandrus, D. & Williams, R. K. Filled skutterudite antimonides: A new class of thermoelectric materials. *Science* **272**, 1325 (1996).

[21] Nolas, G. S., Slack, G. A., Morelli, D. T., Tritt, T. M. & Ehrlich, A. C. The effect of rare-earth filling on the lattice thermal conductivity of skutterudites. *Journal of Applied Physics* **79**, 4002 (1996).

[22] Nolas, G. S., Cohn, J. L. & Slack, G. A. Effect of partial void filling on the lattice thermal conductivity of skutterudites. *Physical Review B* **58**, 164 (1998).

[23] Grytsiv, A. *et al.* Structure and physical properties of the thermoelectric skutterudites $Eu_yFe_{4-x}Co_xSb_{12}$. *Physical Review B* **66**, 094411 (2002).

[24] Morelli, D. T. & Meisner, G. P. Low temperature properties of the filled skutterudite $CeFe_4Sb_{12}$. *Journal of Applied Physics* **77**, 3777 (1995).

[25] Anno, H., Matsubara, K., Notohara, Y., Sakakibara, T. & Tashiro, H. Effects of doping on the transport properties of $CoSb_3$. *Journal of Applied Physics* **86**, 3780 (1999).

[26] Yang, J., Meisner, G. P., Morelli, D. T. & Uher, C. Iron valence in skutterudites: Transport and magnetic properties of $Co_{1-x}Fe_xSb_3$. *Physical Review B* **63**, 014410 (2000).

[27] Yang, J. *et al.* Influence of electron-phonon interaction on the lattice thermal conductivity of $Co_{1-x}Ni_xSb_3$. *Physical Review B* **65**, 094115 (2002).

[28] Yang, J., Endres, M. G. & Meisner, G. P. Valence of Cr in skutterudites: Electrical transport and magnetic properties of Cr-doped $CoSb_3$. *Physical Review B* **66**, 014436 (2002).

Chapter 4

Methodology

In this chapter, density functional theory (DFT), X-ray photoelectron spectroscopy (XPS), and electron energy-loss spectroscopy (EELS) are briefly reviewed.

4.1 Density functional theory

The field of solid state physics is concerned with examining the physical properties of matter in solid phases. Although physics is fundamentally an experimental science, the constant interaction between experiment and theory is an absolute necessity for making progress in understanding the basic properties of the systems under scrutiny. In solid state physics, one studies systems that in principle are well understood within the framework of already established quantum theory. Furthermore, many solids, such as crystals, are well ordered and can be succinctly described mathematically. Although defects in the perfect crystal lattice play a major role in many materials' properties, one would often initially be satisfied to consider idealized models with few or no defects. All in all, calculations of the properties of a material should be within reach.

Unfortunately the reality of the matter proves to be rather more discouraging. Solving the Schrödinger equation quickly becomes intractable for any system of size. For a system of n electrons and N nuclei, the Schrödinger equation depends on $3(n + N)$ variables, three spatial coordinates for each electron and nucleus. For all practical models of a material one usually has

to consider some tens of atoms, which may easily entail more than a hundred electrons. With such a large number of variables this becomes a completely insolvable problem. Some simplification is possible: applying the Born–Oppenheimer approximation allows us to considered nuclear and electronic degrees of freedom separately, and the nuclei can then be seen to supply a *static* background potential in which the electrons move. Although this is a helpful approximation, finding the many electron wave function incorporating the $3n$ electronic degrees of freedom is still an insurmountable problem in most cases [1].

One solution to this problem came as a result of two theorems proposed by Hohenberg and Kohn, which are now known as the Hohenberg–Kohn theorems. These theorems state [1, 2, 3] that *i)* the ground state electron density $\rho_0(\mathbf{r})$ of a system uniquely determines the external potential, and thereby the Hamiltonian and wave function of the system, and *ii)* this ground state electron density can be obtained variationally: the density that gives the minimum system energy is the exact ground state density. In short, these theorems assert that all information available in the wave function is also available in the ground state electron density, and that this density can be found through energy minimization procedures.

The significance of these theorems becomes obvious when one considers that while the wave function itself is dependent on $3n$ variables, the electron density is a function of only three spatial variables. The computational challenge of calculating the properties of a material is thereby greatly reduced. As long as one is able to find the proper *functional* relating the electron density to the property in question, the prediction of materials' properties from first principles should be possible.

One important complicating factor that should be mentioned, is that the exact functional for finding the system energy from the electron density is unknown. The system energy can be expressed as [3]:

$$E_0[\rho_0(\mathbf{r})] = T_{ni}[\rho_0(\mathbf{r})] + V_{ne}[\rho_0(\mathbf{r})] + V_{ee}[\rho_0(\mathbf{r})] + \Delta T[\rho_0(\mathbf{r})] + \Delta V_{ee}[\rho_0(\mathbf{r})] \tag{4.1}$$

Here, the first term is a functional for the kinetic energy of a fictitious system of non-interacting electrons, while the second and third terms are the classical nuclear–electron and electron–electron (Coulombic) interaction. The fourth term is a correction to the kinetic energy due to the electrons interacting, while the final term contains all non-classical corrections to the interaction

energy such as contributions arising from Fermi-statistics. In short, the problem lies with the final two terms in the above equation. These are often treated jointly as an exchange–correlation energy functional, $E_{xc}[\rho_0(\mathbf{r})]$, the exact form of which is unknown. Since the exchange–correlation functional is unknown, various approximations have been developed in an attempt to account for these effects. Even though DFT is in principle variational, thereby allowing us to determine the ground state density through energy minimization, the use of these exchange–correlation approximations introduces an uncertainty. There is no longer any way to be certain that the electron density with the lowest energy is the exact ground state density.

However, comparisons of the calculated electron density with that observed through diffraction experiments show that the correspondence is good for simple materials such as Si and Ge, though there is a larger discrepancy for more complex materials [4, 5, 6]. In practical terms, the most notable failure of modern DFT calculations is a tendency to underestimate the band gap in semiconductors, often by as much as 10–30%. For example, several transition metal oxides that in reality are semiconductors or insulators, are predicted to be metals. These failures are indeed usually ascribed to the the various exchange–correlation approximations that are used.

Most DFT calculations explicitly calculate ground state properties of the system. Therefore, comparison of experimental data with such calculations is often not formally justified as most experiments investigate the system far from the ground state. This is perhaps most obvious with experimental techniques that deliberately bring the system into an excited state, such as the various spectroscopies where energy is absorbed by an electron. The comparison of the ground state density of states with such experiments can be subject to large errors [7, 8].

Despite these challenges, DFT has seen great application and success in many areas of solid state physics and molecular chemistry. In general the geometries and energetics predicted for molecules are in good agreement with observations [3], and the crystal structure, phase stabilities, bulk moduli, heats of formation, and electronic structure of solids are successfully predicted for many solids [9, 10]. In practical terms, calculations based on density functional theory have become an indispensable aid in materials science, and solid state physics and chemistry for interpreting experimental results and predicting materials' properties.

4.2 X-ray photoelectron and Auger electron spectroscopy

X-ray photoelectron spectroscopy (XPS) is a technique for studying the composition, chemical state, and electronic structure of a material by irradiating a sample with X-rays and measuring the kinetic energy of the emitted photoelectrons. Only electrons with binding energy E_b equal to or less than the photon energy $h\nu$ are emitted from the sample, and their binding energy can then be found through the relation $E_b = h\nu - E_k - \phi$. Here ϕ is the instrumental work function and E_k is the measured kinetic energy.

The plot of photoelectron intensity versus binding energy is closely related to the occupied density of states (DOS) of the material. However, since the excitation of a photoelectron generates a core hole, the observed binding energy is not equal to the orbital energy ε. When the core hole is present, the surrounding electrons are rearranged in response to the changed potential at the atom. The binding energy is then given by $E_b = \varepsilon - R$, where R is a relaxation energy taking into account this rearrangement and the effects of the changed potential [11].

In most commercially available XPS instruments, the kinetic energy is analyzed in an electrostatic hemispherical energy analyzer, often reaching a relative energy resolution $\Delta E/E = 5.3 \cdot 10^{-3}$ [12]. Figure 4.1 shows an XPS survey spectrum from a sample consisting of CoP_3 single crystals embedded in a tin-matrix. The spectrum shows sharp peaks from photoelectrons emitted from the energy levels of the various elements in the sample. Also present are peaks from the emitted Auger electrons, these features are discussed further below.

To a first approximation, the binding energy of an electron in a particular atomic orbital is an elemental characteristic, and can be used to identify the elements present in a sample. Furthermore, the peak intensities from the various elements are related to the composition of the sample. Thus, elemental quantification is possible, often with an accuracy of 0.1 at % [13].

XPS is often referred to as a tool for surface characterization. Even though the incident X-rays may penetrate many micrometers into the sample, the majority of the observed photoelectrons originate only a few nanometres below the surface. Still, this may be in the order of 10 unit cells, and is often considered to be sufficient for the signal to be representative for the bulk electronic structure without any effects of the low-dimensionality of the surface. A more pressing problem is the presence of surface contamination such as oxides and hydrocarbons. In order to avoid such problems, the sample is studied in high-vacuum, often after sputtering the surface with ions of

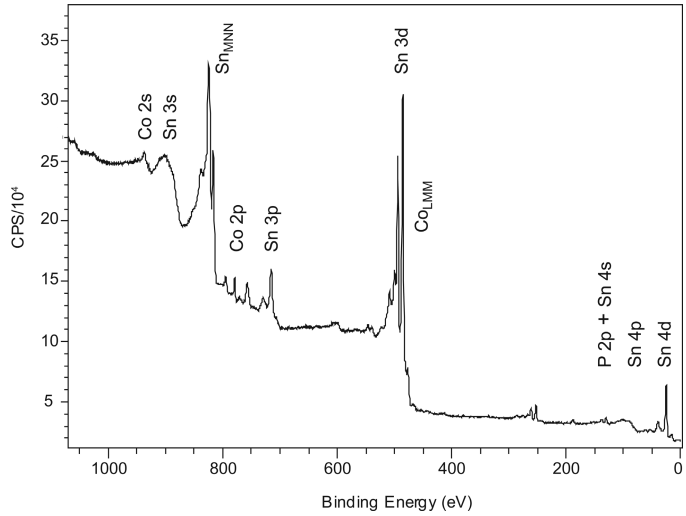

Figure 4.1: *XPS survey scan from a sample consisting of CoP_3 single crystals embedded in a tin matrix.*

argon or xenon.

Although the binding energy is an elemental characteristic, it is affected by the chemical environment of the element. The binding energy E_i of the electron emitted from the energy level i can be described through the equation [13]:

$$E_i = E_{i,0} + kq_i + eV_i \tag{4.2}$$

Here, $E_{i,0}$ is the neutral free atom binding energy, q_i is the charge on the atom in the sample, while V_i is a contribution to the energy due to the charge on the surrounding atoms $V_i = \sum_{j \neq i} \frac{q_j}{r_{ij}}$. If the same element is present in two different chemical environments, a *chemical shift* may be observed:

$$\Delta E_i = k\Delta q_i + e\Delta V_i \tag{4.3}$$

This chemical shift will reflect ground state charge transfer to or from the atom in question, and is an important tool in investigating the electronic structure and bonding in the material. For example, if charge is transferred away from the element when bonds are formed, the intra-atomic screening is reduced giving a higher binding energy. At the same time, the extra-atomic charge may increase. Therefore the two terms in equation (4.3) may have opposite sign, often causing the observed chemical shift to be very small. Thus, accurate measurements of charge transfer through binding energy studies are prone to the uncertainties introduced by a lack of accurate energy referencing due to e.g. charging of the sample. This problem may be somewhat remedied by calibrating the energy scale at known features such as the carbon 1s edge from surface contamination.

In order to reduce the problems associated with energy referencing the concept of the Auger-parameter was introduced by Wagner [14]. As the photoelectron leaves the sample, the atom is left in an excited state with a hole in the orbital that the electron previously occupied. De-excitation occurs with a transition of an electron from a higher energy orbital to the orbital with a hole, and a rearrangement of the valence electrons in response to the core hole (screening). Energy conservation then dictates that the difference in binding energy must be expelled from the atom, either in the form of a photon or — more relevant to our discussion — in the form of yet another excited electron. These are called Auger electrons, and an example of such a process is sketched in figure 4.2. Here, a K shell photoelectron is excited by an incident X-ray photon, leaving a core hole. The atom then is de-excited through a transition of a L_1 electron into the K shell, and the excess energy is transferred to an L_3 electron.

These processes are denoted by the electron shells involved. Under the assumption that the attractive potential of the core holes and extra-atomic environment can be ignored, the kinetic energy of the Auger electron is given by [15]:

$$E_k(KL_1L_3) \approx E_b(K) - E_b(L_1) - E_b(L_3) \tag{4.4}$$

This assumption is not strictly valid, but is acceptable in order to gain a first estimate of the kinetic energy. The kinetic energy of the Auger electron is characteristic for the atomic species in much the same way as the binding energy of the photoelectrons. Furthermore it is independent of the energy of the incident photon, the only requirement being that the incident photon is energetic enough to create the initial core hole.

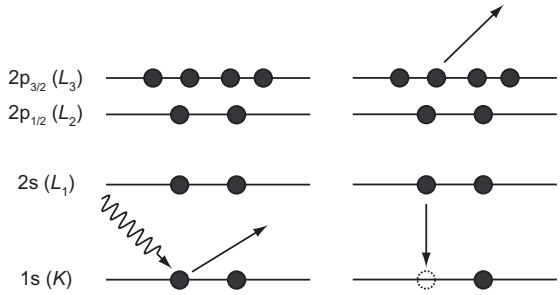

Figure 4.2: *Production of a KL_1L_3 Auger electron. A K shell core hole is generated through absorption of an X-ray photon (left). The atom is then de-excited though the transition of an L_1 electron, filling the core hole and exciting the an L_3 electron (right).*

Wagner realized that the difference between two observed kinetic energies is accurately measurable since any problems with energy referencing due to e.g. sample charging will be cancelled. This led to the definition of the Auger parameter, a modified version of which is given by [16, 17, 11, 18]:

$$\alpha' = E_k(C_1C_2C_3) - E_k(C) + h\nu = E_k(C_1C_2C_3) + E_b(C) \tag{4.5}$$

Here $E_k(C_1C_2C_3)$ is the observed kinetic energy of an Auger electron originating from the process involving the $C_1C_2C_3$ core levels of an element, and $E_k(C)$ and $E_b(C)$ are the kinetic and binding energies of a photoelectron originating from the C orbital of the same atom.

If one assumes that the chemical shift due to ground state charge transfer is the same for all orbitals of an atom, equations (4.5) and (4.4) show that:

$$\begin{aligned} \Delta\alpha' &= \Delta E_k(C_1C_2C_3) + \Delta E_b(C) \\ &= \Delta E_b(C_1) - \Delta E_b(C_2) - \Delta E_b(C_3) + \Delta E_b(C) = 0 \end{aligned} \tag{4.6}$$

Thus, at a first glance, the Auger parameter is insensitive to changes in the core binding energies due to charge transfer. However, the Auger parameter measures the response of the system when

an atom is ionized by removing a core electron. These relaxation effects are more pronounced in the Auger process as there are two core holes that contribute. Therefore often $|\Delta E_k(C_1C_2C_3)| > |\Delta E_b(C)|$, and the Auger parameter shift is nonzero and depends on the response to the core holes.

If Auger parameters for an element are measured in different bonding environments, shifts in the Auger parameter are related to how the bonding affects the response to the core hole. It can be shown that the shift in Auger parameter between two different bonding environments is given by [17]:

$$\Delta\alpha' = \Delta\left[q\frac{dk}{dN} + \left(k - 2\frac{dk}{dN}\right)\left(\frac{dq}{dN}\right) + \frac{dU}{dN}\right] \tag{4.7}$$

Here q is the ground state charge on the atom in question and k is the change in potential when a valence electron is removed. Furthermore, N is core orbital occupation number, and U is the potential from the surrounding atoms. The first term describes the response of the valence electrons to the core hole, while the second and third terms take into account transfer of charge in response to the core hole and the polarization of the surrounding atoms. Thus, equation (4.7) states that changes in the Auger parameter between two chemical environments is caused by differences in response to the core hole. Under certain assumptions, e.g. for metals, the second and third terms in the above equation can be ignored, and equation (4.7) becomes

$$\Delta\alpha' = \Delta q\frac{dk}{dN} \tag{4.8}$$

and the Auger parameter shifts are then directly related to the ground state charge transfer between the two different chemical environments [17].

As an example, figure 4.3 shows the phosphorus 2p-KLL Auger parameter for several phosphorus containing compounds. Significant shifts are observed indicating different degrees of ground state charge transfer in the various compounds.

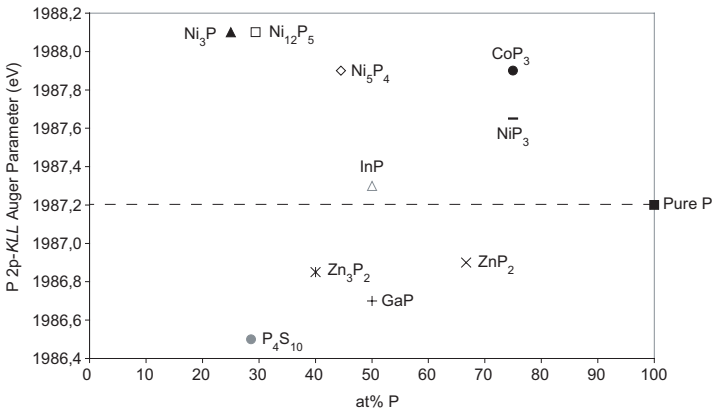

Figure 4.3: *The P 2p-KLL Auger parameter for several compounds.*

4.3 Electron Energy-Loss Spectroscopy

Electrons entering a material may undergo energy losses that contain information about the composition and electronic structure of the sample. Using a nearly monochromatic incident electron beam, these energy losses can be measured with an electron energy-loss spectrometer (EELS). If the experiment is performed in a transmission electron microscope (TEM), the sample is usually only some tens of nanometres thick, and the incident electrons are transmitted through the specimen. After the electrons leave the sample, their energy is measured in a spectrometer, thereby showing how much energy was transferred from the electrons to the specimen.

Figure 4.4 shows a sketch of a so-called post column magnetic prism spectrometer. In practical terms, these spectrometers are attached to the bottom of the TEM, below the viewing screen. The electrons traverse the TEM column from the electron gun, through the sample, and into the the spectrometer through an entrance aperture. Once the electron beam has entered the spectrometer, it is subjected to a uniform magnetic field which acts on the electrons through the Lorentz force $\mathbf{F} = e(\mathbf{v} \times \mathbf{B})$, thereby spatially separating the electrons according to their velocity, i.e. kinetic energy. After passing through a number of electron lenses (not shown in the figure) the electrons arrive at a detector which records the beam intensity as a function of position [19]. Thus, the energy distribution of the electrons may be retrieved.

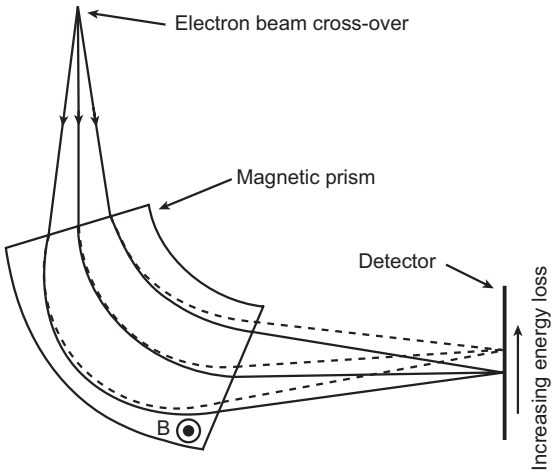

Figure 4.4: *Sketch of a magnetic prism spectrometer. After passing through the sample, the fast electrons enter the magnetic prism, where they are subjected to a uniform magnetic field. This field causes the electrons to be dispersed according to their kinetic energy, and their spatial distribution is recorded by a detector.*

4.3.1 Core excitations

There are several processes by which the incident electrons may transfer energy to the specimen. One of the most important is through excitation of the constituent atoms, whereby the incident electrons impart some energy E and momentum $\mathbf{q}$ to a core electron. The core electron thus makes a transition from an occupied initial state $|\Psi_i\rangle$ to an unoccupied final state $|\Psi_f\rangle$ above the Fermi–level, see figure 4.5.

In order for this transition to occur, the core electron must according to the Pauli exclusion principle receive an amount of energy $E \geq E_F - E_C$, where E_F is the Fermi-energy and E_C is the binding energy of the core level. In the energy loss spectrum, sharp features may be observed at the threshold energy signaling the onset of these transitions. The electron energy-loss spectrum measures the probability that such excitations occur, and reflects a convolution of the occupied part of the DOS with the unoccupied part.

The probability that an electron in an initial state $|\Psi_i\rangle$ will be scattered into one of the final states $|\Psi_f\rangle$ is given by the double differential cross-section [20]:

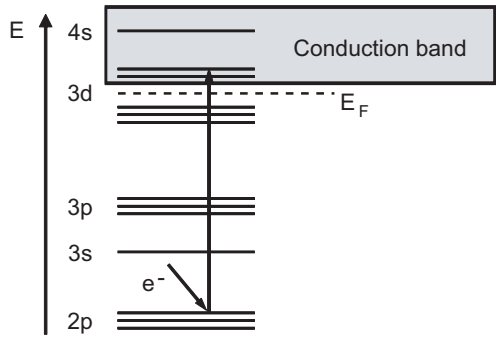

Figure 4.5: *Sketch of an EELS excitation process. The incident electron transfers energy to a 2p core electron, which is then excited into an empty 3d state above the Fermi-level.*

$$\begin{aligned}\frac{\mathrm{d}^2\sigma(E,\mathbf{q})}{\mathrm{d}E\,\mathrm{d}\mathbf{q}} &\propto \frac{4\gamma^2}{a_0^2\mathbf{q}^4}\sum_f |\langle\Psi_f|e^{i\mathbf{q}\cdot\mathbf{r}}|\Psi_i\rangle|^2 \\ &= \frac{4\gamma^2}{a_0^2\mathbf{q}^4}\rho(E_i+E)|\langle\Psi_f|e^{i\mathbf{q}\cdot\mathbf{r}}|\Psi_i\rangle|^2 \end{aligned} \tag{4.9}$$

Here a_0 is the the Bohr radius and γ the relativistic correction factor. The final and initial states are chosen so that the difference in their energies $E_f - E_i$ equals the energy loss E of the incident electron. There can be many possible final states for the electron; under the assumption that the matrix element term $|\langle\Psi_f|e^{i\mathbf{q}\cdot\mathbf{r}}|\Psi_i\rangle|^2$ is a constant for the scattering process in question, the multiple final states can be accounted for by the sum in the first line of equation (4.9), giving the DOS term $\rho(E_i + E)$ in the final expression.

The exponential appearing in the matrix element term $|\langle\Psi_f|e^{i\mathbf{q}\cdot\mathbf{r}}|\Psi_i\rangle|^2$ can be expanded in a Taylor series:

$$e^{i\mathbf{q}\cdot\mathbf{r}} = 1 + i\mathbf{q}\cdot\mathbf{r} + \frac{(i\mathbf{q}\cdot\mathbf{r})^2}{2!} + \cdots \tag{4.10}$$

In most experiments the majority of electrons transfer only a small amount of momentum to the sample, and any contribution to the spectrum from electrons undergoing a large momentum

transfer may further be limited using an angle limiting collection aperture in front of the spectrometer. In this case, the product $\mathbf{q} \cdot \mathbf{r}$ is small and the Taylor expansion can be truncated after the second term. Inserting the Taylor expansion into equation (4.9) and remembering that the initial and final states are orthogonal to each other, we then get:

$$\frac{\mathrm{d}^2\sigma(E,\mathbf{q})}{\mathrm{d}E\,\mathrm{d}\mathbf{q}} \propto \frac{4\gamma^2}{a_0^2\mathbf{q}^4}\rho(E_i+E)|\langle\Psi_f|i\mathbf{q}\cdot\mathbf{r}|\Psi_i\rangle|^2 \tag{4.11}$$

The limit of small $\mathbf{q}$ is called the dipole approximation. If valid, the electronic transitions are limited to those with a change in orbital angular momentum quantum number $\Delta l = \pm 1$, similar to the transitions that take place upon absorption of a photon. In this case, the DOS term in equation (4.11) should be interpreted as an angular momentum (symmetry) selected DOS, while the matrix term $|\langle\Psi_f|i\mathbf{q}\cdot\mathbf{r}|\Psi_i\rangle|^2$ takes into account the radial overlap of the initial and final states. For moderate to high energy loss transitions, the initial states are essentially atomic and are strongly localized near the atomic core. Non-zero values for the overlap are therefore only achieved for final states localized on the same atom. Thus, the intensity and shape of a peak in the energy loss spectrum represents a site and symmetry selected density of unoccupied states. Furthermore, the energy loss intensities for high energy transitions is reduced as the spatial overlap of the initial and final states is small for large differences in binding energy.

This interpretation is a useful first approximation in understanding the features observed in the energy-loss spectrum. However, it should be noted that, as with photoelectron spectroscopy, a core hole is generated when the excitation occurs. As a consequence the potential felt by the surrounding electrons is changed, and the final states $|\Psi_f\rangle$ are not those found in the ground state. These effects are important when comparing observed energy-loss spectra with calculations.

While the initial states are located close to the core and are mainly atomic in nature, the final states are further from the core and located above the Fermi-level. The energy-loss spectrum will therefore reflect the valence electron configuration of the atom. An example of this can be seen in figure 4.6(a), which shows the energy-loss features (called 'white lines') due to the $L_{2,3}$ excitations in the first row transition metals. These features appear when transition metal (TM) 2p electrons are excited into the empty 3d and 4s states. The radial overlap of the 2p and 4s states is small compared to that of the 2p and 3d states [21], and the transition probability is therefore dominated by the 2p→3d transitions. When moving from Ti, with a valence electron configuration [Ar]$3d^2 4s^2$, towards Cu, [Ar]$3d^{10} 4s^1$, the 3d states are gradually filled by additional

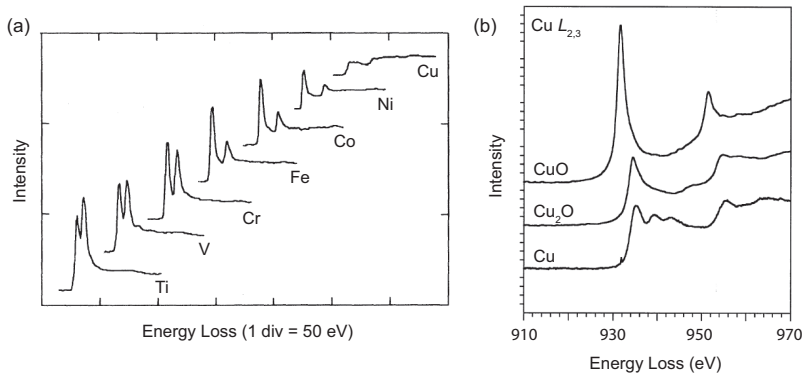

Figure 4.6: *The $L_{2,3}$ edges of (a) seven pure transition metal films, adapted from Pearson [23] and (b) Cu in pure copper and its oxides, adapted from Keast [24].*

valence electrons. As the number of available states above the Fermi-level decreases, the sharp, intense peaks observed for Ti are reduced, until virtually no such peaks are observed in Cu [22, 23]. Indeed, it has been shown that with appropriate normalization and correction for the matrix element of equation (4.11), the total white line intensity is linearly correlated to the number of 3d holes [23].

The final states are heavily influenced by the interaction with the neighbouring atoms, and are therefore strongly affected by the bonding and coordination of the excited atom. A most dramatic example of this is the case of copper and its oxides. Figure 4.6(b) shows the $L_{2,3}$ edges of Cu, Cu_2O, and CuO. As already mentioned, the white lines are almost completely absent in pure copper, as the 3d band is completely filled. However, upon oxidation, the sharp peaks associated with the 2p→3d transitions are readily observed. This is interpreted as an emptying of the Cu 3d states upon bonding with oxygen, consistent with an ionic model where charge is transferred from copper to oxygen. This approach has proven useful in studying the alloying behaviour of compounds containing transition metals [25, 26].

4.3.2 Collective excitations and the joint density of states

As mentioned previously, the energy-loss spectrum is related to a convolution of initial states with final states. However, the above treatment explicitly refrains from treating the energy distribution

of initial states. This is adequate in the case of energy losses associated with the excitation of core electrons. The initial states of these transitions are usually sharply localized in energy, and the spectrum can be interpreted as a convolution of the final states with delta-function-like initial states.

However, for transitions where both the initial and final states are located close to the Fermi-level, this treatment is no longer sufficient. The initial states are then highly distributed in energy, and for any given energy loss there are several possible transitions. In this case the convolution must be treated explicitly, and the observed energy-loss intensity can be described by [20]:

$$I(E) \propto \int_{E_F-E}^{E_F} |\langle \Psi_f | e^{i\mathbf{q}\cdot\mathbf{r}} | \Psi_i \rangle|^2 \rho(E_i + E)\rho(E_i)\mathrm{d}E_i \tag{4.12}$$

where the integral is over all initial state with energy between E_F and $E_F - E$. Thus, this energy-loss spectrum should be considered as reflecting a *joint density of states* of the material, and not just the DOS above the Fermi-level. As both the initial and final states are located close to the Fermi-level, they are heavily influenced by the bonding arrangements in the material, and the low loss EELS spectrum may contain much useful information.

The low loss spectrum is, however, not dominated by these single electron transitions. Rather, the most intense features visible are usually the so-called plasmons. As the incident electron enters the material, the electric field surrounding it repulses the electrons in the material, forcing the electron distribution out of equilibrium with regard to the atomic potential. After the electron has left the material, the restoring force between the electrons and nuclei cause a collective oscillation of the valence electrons about the equilibrium position.

A good understanding of this phenomenon can be achieved by studying the macroscopic equations of electrodynamics. If a material is subjected to an oscillating external electric field $\mathbf{E}(\omega, \mathbf{k})$, we know from classical electrodynamics that it is polarized according to [27]:

$$\mathbf{P}(\omega, \mathbf{k}) = \varepsilon_0 \left[\varepsilon(\omega, \mathbf{k}) - 1\right] \mathbf{E}(\omega, \mathbf{k}) \tag{4.13}$$

where $\varepsilon(\omega, \mathbf{k}) = \varepsilon_1 + i\varepsilon_2$ is the complex dielectric function of the material, with real and imaginary parts ε_1 and ε_2. The electric displacement of the medium is given by

$$\begin{aligned}\mathbf{D}(\omega,\mathbf{k}) &= \varepsilon_0\mathbf{E}(\omega,\mathbf{k}) + \mathbf{P}(\omega,\mathbf{k}) \\ &= \varepsilon_0\mathbf{E}(\omega,\mathbf{k}) + \varepsilon_0\left[\varepsilon(\omega,\mathbf{k}) - 1\right]\mathbf{E}(\omega,\mathbf{k}) = \varepsilon(\omega,\mathbf{k})\varepsilon_0\mathbf{E}\end{aligned} \tag{4.14}$$

We notice that the polarization exactly cancels the external field when $\varepsilon(\omega) = 0$. In the free electron model, the electrons act as an oscillating plasma, and it can be shown [28] that this resonance frequency, called the plasma frequency, is given by:

$$\omega_p = \sqrt{\frac{Ne^2}{Vm_0\varepsilon_0}} \tag{4.15}$$

where N is the number of valence electrons in the unit cell, V is the unit cell volume, ε_0 is the permittivity of free space, e the electron charge, and m_0 the free electron mass.

Simple metals and semi-conductors such as Be, B, Al, Ge, GaAs, and Si display sharp and prominent plasmon peaks, and peaks at multiples of the plasmon energy due to the incident electron exciting several plasmons before leaving the sample. As an example, the low loss spectrum from Si is shown in figure 4.7 where the energy loss peaks from three plasmon excitations are readily observed. In the case of such materials, the free electron model is quite successful in predicting the plasmon energy $E_p = \hbar\omega_p$ [29, 19].

On the other hand, wide band gap ionic materials and elemental materials of transition metals tend to exhibit broad plasmon peaks, with only the first plasmon visible, as exemplified by the low loss spectrum of Co in figure 4.7. In these materials it is not adequate to describe the valence electrons as a free electron plasma with a single, common, resonance frequency. Additionally, there is often no obvious choice for the number of contributing valence electrons, and the simple Drude model may fail dramatically to give adequate estimates of the plasmon energy.

In the dielectric formulation, the double differential cross section is given by [19, 20]:

$$\frac{\mathrm{d}^2\sigma}{\mathrm{d}\Omega\mathrm{d}E} = \frac{1}{\pi^2 a_0 m_0 v^2 n_a}\frac{1}{\Theta^2 + \Theta_E^2}\mathrm{Im}\left(\frac{-1}{\varepsilon(E,\mathbf{q})}\right) \tag{4.16}$$

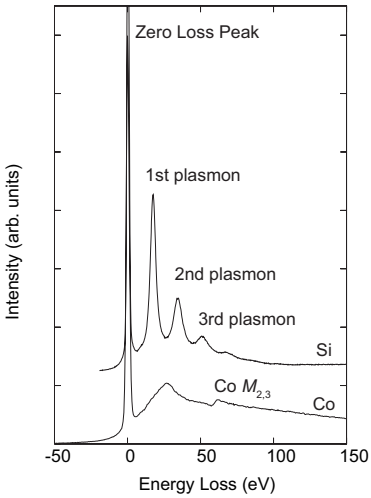

Figure 4.7: *The low loss region of Si and Co. In the case of simple metals and semi-conductors, multiple, sharp plasmon peaks are usually observed in the low loss region, as is the case for Si seen in the figure. For more complex metals such as Co a single broad peak is observed. Also seen is the Co $M_{2,3}$ edge at approximately 60 eV.*

Here a_0 is the Bohr-radius, m_0 the electron mass, v the speed of the incident electron, and n_a the number of atoms per unit volume. In addition, Θ and Θ_E are the scattering angle of the electron, and characteristic angle for an energy loss E [19]. The final term is referred to as the loss function and can be interpreted as a renormalization of imaginary part of the dielectric function:

$$\mathrm{Im}\left(\frac{-1}{\varepsilon(E,\mathbf{q})}\right) = \frac{\varepsilon_2}{\varepsilon_1^2+\varepsilon_2^2} \tag{4.17}$$

Through equation (4.16) the close connection between the observed energy loss spectrum and the imaginary part of the dielectric function is established, and the full dielectric function can the be retrieved through a Kramers–Kronig analysis [27]. As an example, figure 4.8 shows a comparison of the dielectric function obtained from EELS experiments, with the dielectric function from DFT calculations.

There are several advantages to using this approach to determine the dielectric function as compared to traditional optical methods. EELS experiments are be expected to be less sensitive

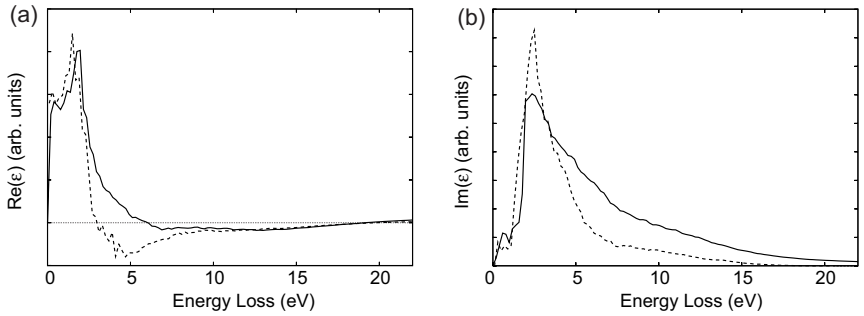

Figure 4.8: *(a) The real and (b) imaginary parts of the dielectric function of $CoAs_3$ as obtained from EELS and DFT. The experimentally obtained function is shown with a fully drawn line, while the theoretical function is a dashed line. From Prytz* et al. *[30].*

to surface contamination than e.g. optical reflectance experiments, and may yield the dielectric function over a wider energy (frequency) range, although with poorer energy resolution.

To summarize, in the initial study of new materials, only small amounts may be readily available. Thus, measurements of e.g. thermoelectric properties may at first be difficult and unrealiable. However, after having determined the crystal structure and thermal parameters by diffraction techniques, the electronic structure can be studied combining DFT calculations and experimental studies using advanced analytical TEM. This instrument is highly versatile with the opportunity of performing EELS, precise convergent beam electron diffraction and electron holography. These techniques can be used on small volumes of materials to determine their electronic structure and bonding, from which their thermoelectric properties can be inferred. Thus, these TEM based techniques may be of great value when searching for new materials.

References

[1] Kohn, W. Nobel lecture: Electronic structure of matter—wave functions and density functionals. *Review of Modern Physics* **71**, 1253 (1999).

[2] Hohenberg, P. & Kohn, W. Inhomogeneous electron gas. *Physical Review* **126**, B864 (1964).

[3] Cramer, C. J. *Essentials of Computational Chemistry – Theories and Models*, chap. 8, 233–273 (John Wiley and Sons Ltd., Chichester, 2002).

[4] Zuo, J. M., Kim, M., O'Keeffe, M. & Spence, J. C. H. Direct observation of d-orbital holes and Cu–Cu bonding in Cu_2O. *Nature* **401**, 49 (1999).

[5] Zuo, J. M. Measurements of electron densities in solids: a real-space view of electronic structure and bonding in inorganic crystals. *Reports on Progress in Physics* **67**, 2053 (2004).

[6] Wu, L. *et al.* Valence-electron distribution in MgB_2 by accurate diffraction measurements. *Physical Review B* **69**, 064501 (2004).

[7] Lie, K., Brydson, R. & Davock, H. Band structure of TiB2: Orientation-dependent EELS near-edge fine structure and the effect of the core hole at the B K edge. *Physical Review B* **59**, 5361 (1999).

[8] Lie, K., Høier, R. & Brydson, R. Theoretical site- and symmetry-resolved density of states and experimental EELS near-edge spectra of AlB2 and TiB2. *Physical Review B* **61**, 1786 (2000).

[9] Sutton, A. P. *Electronic structure of materials*, chap. 11, 204–214 (Oxford University Press, Oxford, 1993).

[10] Hafner, J. Atomic-scale computational materials science. *Acta Materialia* **48**, 71 (2000).

[11] Thompson, M., Baker, M. D., Christie, A. & Tyson, J. F. *Auger Electron Spectroscopy*, vol. 74 of *Chemical Analysis* (John Wiley and Sons, New York, 1985).

[12] Drummond, I. W. XPS: Instrumentation and performance. In Briggs, D. & Grant, J. T. (eds.) *Surface analysis by Auger and X-ray photoelectron spectroscopy*, chap. 5, 117–144 (IM Publications and SurfaceSpectra Limited, Charlton and Manchester, 2003).

[13] Grant, J. T. XPS: Basic principles, spectral features and qualitative analysis. In Briggs, D. & Grant, J. T. (eds.) *Surface analysis by Auger and X-ray photoelectron spectroscopy*, chap. 2, 31–56 (IM Publications and SurfaceSpectra Limited, Charlton and Manchester, 2003).

[14] Wagner, C. D. Chemical shifts of auger lines, and the auger parameter. *Faraday Discussions of the Chemical Society* **60**, 291 (1975).

[15] Grant, J. T. AES: Basic principles, spectral features and qualitative analysis. In Briggs, D. & Grant, J. T. (eds.) *Surface analysis by Auger and X-ray photoelectron spectroscopy*, chap. 3, 57–88 (IM Publications and SurfaceSpectra Limited, Charlton and Manchester, 2003).

[16] Moretti, G. The auger parameter. In Briggs, D. & Grant, J. T. (eds.) *Surface analysis by Auger and X-ray photoelectron spectroscopy*, chap. 18, 501–530 (IM Publications and SurfaceSpectra Limited, Charlton and Manchester, 2003).

[17] Thomas, T. D. & Weightman, P. Valence electron structure of AuZn and AuMg alloys derived from a new way of analyzing Auger-parameter shifts. *Physical Review B* **33**, 5406 (1986).

[18] Gaarenstroom, S. W. & Winograd, N. Initial and final state effects in the ESCA spectra of cadmium and silver oxides. *The Journal of Chemical Physics* **67**, 3500 (1977).

[19] Egerton, R. F. *Electron Energy Loss Spectroscopy in the Electron Microscope* (Plenum Press, New York, 1986), 1 edn.

[20] Rez, P. Energy loss fine structure. In Ahn, C. C. (ed.) *Transmission Electron Energy Loss Spectrometry in Materials Science and the EELS Atlas*, chap. 4, 97–126 (Wiley-VCH Verlag GmbH & Co. KGaA, Weinheim, 2004).

[21] Muller, D. A., Singh, D. J. & Silcox, J. Connections between the electron-energy loss spectra, the local electronic structure, and the physical properties of a material: A study of nickel aluminum alloys. *Physical Review B* **57**, 8181 (1998).

[22] Leapman, R. D., Grunes, L. A. & Fejes, P. L. Study of the $L_{2,3}$ edges in the $3d$ transition metals and their oxides by electron-energy loss spectroscopy with comparison to theory. *Physical Review B* **26**, 614 (1982).

[23] Pearson, D. H., Ahn, C. C. & Fultz, B. White lines and d-band occupancies for the $3d$ and $4d$ transition metals. *Physical Review B* **47**, 8471 (1993).

[24] Keast, V. J., Scott, A. J., Brydson, R., Williams, D. B. & Bruley, J. Electron energy-loss near edge structure – a tool for the investigastion of electronic structure on the nanometre scale. *Journal of Microscopy* **203**, 135–175 (2001).

[25] Ouyang, H. & Jen-Tai, K. Occupancy of the $3d$ electron shell of Co and Cr in nanosized CoCrPt magnetic thin films. *Journal of Applied Physics* **92**, 7510 (2002).

[26] Pearson, D. H., Ahn, C. C. & Fultz, B. Measurements of $3d$ occupancy from $L_{2,3}$ electron energy-loss-spectroscopy spectra of rapidly quenched CuZr, CuTi, CuPd, CuPt and CuAu. *Physical Review B* **50**, 12969 (1994).

[27] Yu, P. Y. & Cardona, M. *Fundamentals of Semiconductors* (Springer-Verlag, Berlin, 2003), 3 edn.

[28] Kittel, C. *Introduction to Solid State Physics* (John Wiley & Sons, Inc., 1996), 7th edn.

[29] Raether, H. *Excitation of Plasmons and Interband Transitions by Electrons*, vol. 88 of *Springer Tracts in Modern Physics* (Springer-Verlag, Berlin, 1980).

[30] Prytz, Ø., Løvvik, O. M. & Taftø, J. Comparison of theoretical and experimental dielectric functions: Electron energy-loss spectroscopy and density-functional calculations on skutterudites. *Physical Review B* **74**, 245109 (2006).

Chapter 5

Overview of papers

The scientific results of this Ph.D. study are presented in the four papers included in this thesis. The main methods used are density-functional theory, electron energy-loss spectroscopy, and x-ray photoelectron spectroscopy. A brief summary of the articles is given below.

Paper I

As discussed in a previous chapter, filling the voids in the skutterudite structure can dramatically decrease the thermal conductivity of the material. Based on the rattling box picture of this effect, it can be expected that the magnitude depends on the the size of the filling atom relative to the size of the void: a relatively small atom will decrease the thermal conductivity more than a relatively large atom [1].

This paper investigates the crystal structure, thermodynamic stability, and electronic structure of La-, Y-, and Sc-filled CoP_3 using density functional theory (DFT). While these elements are chemically similar, they have different atomic radii, with Sc the smallest and La the largest. It can therefore be expected that filling the structure with Sc would have a greater effect on the thermal conductivity than filling with La.

The solubility of La, Y, and Sc in CoP_3 is calculated to be around 5, 3-6 %, and below 1% at 0 K, respectively. Although these are rather small values, this is expected to increase considerably

if Fe is substituted for Co. Calculations of the density of states and band structure indicate that the main effect of filling is to push the Fermi-level into the conduction band, while other features remain rather unchanged.

Paper II

In this article, the possibility of combining density functional theory (DFT) and electron energy loss spectroscopy (EELS) to determine the dielectric function of materials is investigated. The binary skutterudites CoP_3, $CoAs_3$, and $CoSb_3$ serve as model systems, and the theoretically and experimentally obtained low energy-loss spectra and plasmon energies are compared.

The skutterudites display multiple sharp plasmon peaks, similar to those observed in simple metals and semiconductors. When compared with the plasmon energies calculated using the free electron model, the experimental plasmons are found at systematically higher energy.

The DFT calculated plasmon energy also deviates significantly from the observed values, but in a non-systematic way. While the plasmon energy of CoP_3 and $CoAs_3$ is underestimated, the calculated value for $CoSb_3$ is overestimated by more that 6 %. This is contrary to what the case of some crystals with less complicated electronic structure, where good agreement is found [2]. When the theoretical and experimental low loss region below the plasmon peaks are compard, a qualitative agreement is obtained for the skutterudites.

In the case of $CoAs_3$, a Kramers–Kronig analysis of the EELS spectra gives a dielectric function in good agreement with the theoretic calculations. Some of the remaining discrepancies may be caused by the challenge of refining the experimental spectra before Kramers–Kronig analysis.

Paper III

While a predominantly covalent bonding is expected in the binary skutterudites, a partial ionic character cannot be discounted. In this paper, the transition-metal 3d occupancy of a series of thermoelectric skutterudites is investigated using electron energy-loss spectroscopy.

The intensity of the transition-metal $L_{2,3}$ edges of CoP_3, $CoAs_3$, $CoSb_3$, and NiP_3 are investi-

gated and compared those of the pure metals. In the case of the cobalt based skutterudites, a significant increase of the edge intensity is observed, the largest change is observed in the case of CoP_3. Previous studies have shown that the intensity of these edges correlates with the 3d occupancy [3]. Based on this it concluded that there is an emptying of the 3d states in these materials compared to the situation in pure metals. The reduction in 3d occupancy is 0.77 electrons/atom for CoP_3, and about 0.4 electrons/atom for the arsenic and antimony based skutterudites. Only small changes in occupancy are observed for NiP_3.

In comparison, the intensity of the $L_{2,3}$ edges of iron in $LaFe_4P_{12}$ is significantly decreased, signalling a filling of the 3d states. This is consistent with the idea that each interstitial La atom (rattler) donates three electrons to compensate for missing valence electron of iron as compared to cobalt, and indicates that the compensation mainly takes place on the iron site.

Paper IV

In this article, the Auger parameter is used to study the valence electron distribution in CoP_3. The electron transfer between Co and P is estimated using the model of Thomas and Weightman [4] which relates changes in Auger parameter values to charge transfer. In the EELS study presented in Paper III, an emptying of the cobalt 3d states was found. Here it is found that each phosphorus atom gains approximately 0.24 electrons. Based on stoichiometric considereations, this is equivalent to a donation from cobalt of about 0.72 electrons/atom, which is in excellent agreement with the EELS studies of Paper III.

References

[1] Uher, C. Skutterudites: Prospective novel thermoelectrics. *Semiconductors and semimetals* **69**, 139 (2001).

[2] Keast, V. J. Ab initio calculations of plasmons and interband transitions in the low-loss electron energy-loss spectrum. *Journal of Electron Spectroscopy and related phenomena* **143**, 97 (2005).

[3] Pearson, D. H., Ahn, C. C. & Fultz, B. White lines and d-band occupancies for the $3d$ and $4d$ transition metals. *Physical Review B* **47**, 8471 (1993).

[4] Thomas, T. D. & Weightman, P. Valence electron structure of AuZn and AuMg alloys derived from a new way of analyzing Auger-parameter shifts. *Physical Review B* **33**, 5406 (1986).